*remote sensing*

MDPI

*Article*

# High-Resolution Collaborative Forward-Looking Imaging Using Distributed MIMO Arrays

**Shipei Shen [1,2], Xiaoli Niu [1], Jundong Guo [1], Zhaohui Zhang [1] and Song Han [1,*]**

[1] Aerospace Information Research Institute, Chinese Academy of Sciences, Beijing 100190, China; shenshipei22@mails.ucas.ac.cn (S.S.); niuxl@aircas.ac.cn (X.N.); guojd@aircas.ac.cn (J.G.); zhangzh400268@aircas.ac.cn (Z.Z.)

[2] School of Electronic, Electrical and Communication Engineering, University of Chinese Academy of Sciences, Beijing 100049, China

* Correspondence: hansong@aircas.ac.cn

**Abstract:** Airborne radar forward-looking imaging holds significant promise for applications such as autonomous navigation, battlefield reconnaissance, and terrain mapping. However, traditional methods are hindered by complex system design, azimuth ambiguity, and low resolution. This paper introduces a distributed array collaborative, forward-looking imaging approach, where multiple aircraft with linear arrays fly in parallel to achieve coherent imaging. We analyze signal model characteristics and highlight the limitations of conventional algorithms. To address these issues, we propose a high-resolution imaging algorithm that combines an enhanced missing-data iterative adaptive approach with aperture interpolation technique (MIAA-AIT) for effective signal recovery in distributed arrays. Additionally, a novel reference range cell migration correction (reference RCMC) is employed for precise range–azimuth decoupling. The forward-looking algorithm effectively transforms distributed arrays into a virtual long-aperture array, enabling high-resolution, high signal-to-noise ratio imaging with a single snapshot. Simulations and real data tests demonstrate that our method not only improves resolution but also offers flexible array configurations and robust performance in practical applications.

**Keywords:** airborne forward-looking radar; distributed coherent aperture radar (DCAR); range cell migration correction (RCMC); iterative adaptive approach (IAA); missing data recovery

check for updates

**Citation:** Shen, S.; Niu, X.; Guo, J.; Zhang, Z.; Han, S. High-Resolution Collaborative Forward-Looking Imaging Using Distributed MIMO Arrays. *Remote Sens.* **2024**, *16*, 3991. https://doi.org/10.3390/rs16213991

Academic Editors: Yin Zhang, Deqing Mao, Yulin Huang and Yachao Li

Received: 1 September 2024
Revised: 15 October 2024
Accepted: 23 October 2024
Published: 27 October 2024

**Copyright:** © 2024 by the authors. Licensee MDPI, Basel, Switzerland. This article is an open access article distributed under the terms and conditions of the Creative Commons Attribution (CC BY) license (https://creativecommons.org/licenses/by/4.0/).

## 1. Introduction

Airborne forward-looking radar imaging technology provides high-resolution, all-weather, long-range imaging capabilities, making it ideal for precision guidance, battlefield reconnaissance, and terrain mapping [1–5]. Given its broad range of practical uses, this technology is increasingly becoming a focal point in radar imaging research. Traditionally, radar imaging techniques like monostatic synthetic aperture radar (SAR) [6,7] and Doppler beam sharpening (DBS) [8,9] are primarily designed for side-looking areas along the flight trajectory. These methods utilize Doppler information generated by the relative movement between the radar platform and the target to achieve high azimuth resolution. However, in forward-looking scenarios, these conventional techniques face considerable challenges. Targets aligned symmetrically along the flight path share identical Doppler histories, and the forward-looking region experiences a minimal Doppler frequency gradient, complicating the attainment of high-resolution, unambiguous azimuth imaging [10] .

Several innovative techniques have been explored to enhance azimuth imaging performance in forward-looking regions. Monopulse forward-looking imaging estimates the target's angle by comparing signal differences across multiple antennas [11]. This technique provides accurate angular resolution for isolated strong targets within the beam, but its performance declines when multiple targets are present, as signals from different targets interfere with each other, making it difficult to resolve them simultaneously. On the other

hand, real beam scanning involves mechanically or electronically steering the radar beam across the forward-looking region to gather two-dimensional images [12]. This method, commonly used in systems like the APN-241 radar, is straightforward and provides real-time imaging capabilities. However, its resolution deteriorates rapidly as the distance to the target increases. To address the limitations of real beam scanning, large-aperture array imaging uses multiple antennas arranged along the flight path, effectively increasing the aperture and enhancing angular resolution, and is known as forward-looking array SAR [13–15]. This method significantly improves resolution. However, the size and weight constraints of airborne platforms limit the physical aperture that can be achieved, and thus the full potential of this method remains restricted.

Another promising approach is bistatic forward-looking SAR, which separates the transmitter and receiver platforms, creating a larger virtual aperture that enhances resolution [16–19]. By avoiding the alignment issues between range and Doppler gradient directions, bistatic SAR enables unambiguous imaging in forward-looking regions. However, this technique demands precise synchronization between the platforms, and the complexity of motion compensation remains a significant challenge.

Super-resolution techniques have been widely studied to improve forward-looking radar imaging resolution. Inverse filtering recovers high-frequency details but is sensitive to noise, leading to instability in low SNR environments [20,21]. In contrast, Bayesian super-resolution techniques offer a more robust alternative by incorporating statistical priors about the target and noise distributions [22,23]. Regularization techniques, such as Tikhonov and sparse regularization, stabilize the inversion process, with sparse methods preserving sharp edges [24,25]. Additionally, spectral estimation methods like MUSIC and Capon beamforming can resolve targets beyond the Rayleigh limit but require multiple snapshots, which is challenging for fast-moving platforms. The iterative adaptive approach (IAA) mitigates this limitation by enabling effective imaging with fewer samples [26,27].

Analysis of existing forward-looking methods reveals that increasing azimuth aperture length is a crucial strategy for enhancing imaging performance. However, platform payload constraints make achieving a sufficiently long azimuth aperture with a single airborne platform challenging. Fortunately, recent research has proposed distributed coherent aperture radar (DCAR) systems to overcome the limitation, offering valuable insights [28–32]. As a novel radar architecture, distributed coherent aperture radar disperses multiple apertures spatially and synthesizes electromagnetic wave energy in space, significantly enhancing radar system detection range and measurement precision. In [30], experiments using distributed X-band phased array radar to track aircraft targets demonstrated a 9 dB improvement in the signal-to-noise ratio. Additionally, employing sparse reconstruction algorithms in FMCW-based vehicular multi-transmit and multi-receive (MIMO) distributed radar imaging has proven effective in enhancing forward-looking imaging resolution for vehicles [32].

In distributed coherent radar systems, precise time, phase, and frequency synchronization is essential for proper subarray operation, as any discrepancies degrade imaging and detection performance [33]. Synchronization methods are categorized into hardware- and software-based solutions [34]. A common hardware approach is the self-mixing circuit using a two-tone waveform, which ensures high-precision synchronization but increases system complexity and depends on a master node [35,36]. In contrast, software methods, such as GPS-based solutions, are more flexible, using digital processing to achieve high precision without extra hardware [37,38]. In this study, synchronization is achieved using GPS, BeiDou, and rubidium atomic clocks, providing a time accuracy better than 2 ns, frequency stability better than $8 \times 10^{-12}$/s, and phase noise below $-157$ dBc@1KHz. These values are also used as settings in the subsequent simulation tests.

In addition to system synchronization, the impact of platform motion errors must be considered in distributed airborne systems. Platform motion errors can cause phase center shifts among array elements and beam pointing deviations, leading to significant defocusing in the final cooperative imaging results. Motion compensation is essential and

varies across forward-looking imaging models. For instance, bistatic SAR models use a two-step compensation to correct range-independent and range-dependent errors [39], while single-array systems rely on motion measurement information for error modeling and compensation [40]. For the current model, existing algorithms are insufficient, but single-array compensation methods can be applied first, followed by inter-array error correction. The inter-array error correction can draw upon relevant compensation algorithms used in distributed coherent radar systems. For coherent distributed array imaging with unknown position perturbations, reference [41] used sparse constraints and data consistency analysis for phase error compensation, progressively correcting antenna position deviations to restore clear target images despite significant disturbances.

In light of these advancements, this paper proposes a new imaging model in which multiple airborne platforms equipped with linear arrays collaboratively image the forward region. This model significantly diverges from existing airborne imaging models by introducing the concept of the distributed coherent aperture into airborne forward-looking imaging. The primary differences include the discontinuity issues in azimuth signals sampled by the distributed array and the unique range migration characteristics of this system. For azimuth signals from distributed arrays, spatial sampling by distinct arrays on the same target is discontinuous and presents considerable gaps. Traditional focusing methods and range cell migration correction techniques are not applicable to this model, and thus fail to achieve high-resolution forward-looking imaging results. To address these challenges, we first propose a novel range cell migration correction method called reference RCMC, which is specifically designed for distributed coherent array collaborative imaging. By implementing stepwise correction based on a reference array, the impact on subsequent algorithms for predicting discontinuous signals is reduced. Building on this foundation, we treat the azimuth discontinuity in distributed arrays as a signal with missing samples problem. For this issue, considering the impact of platform jitter, directly applying methods such as compressed sensing for sparse imaging in a distributed array system yields suboptimal results. Fortunately, the signals from each subarray are relatively stable. Thus, the MIAA algorithm can be individually applied to each subarray for predictive extrapolation of azimuth gaps [42,43]. Subsequently, aperture extrapolation and interpolation techniques are used to perform weighted superposition of the extrapolated results from different arrays, effectively predicting and filling in the missing signals to form a long-aperture virtual array [44]. Upon completing the aforementioned operations, traditional SAR algorithms and distortion correction are finally employed to achieve stable, high-resolution joint imaging of the distributed array. Simulation and experimental results demonstrate that this method can achieve high-resolution, forward-looking imaging with a distributed array system. The main contributions of this paper are summarized as follows:

1. Proposal of a novel airborne distributed array collaborative, forward-looking imaging model, offering a new perspective for forward-looking imaging methods.
2. Development of a new forward-looking imaging algorithm for this model. The algorithm transforms the distributed array imaging problem into a signal sampling loss recovery problem. Utilizing the improved MIAA-AIT algorithm, it converts the distributed array sampling signals into virtual long-aperture sampling signals, effectively enhancing the signal-to-noise ratio and achieving high-resolution forward-looking imaging in a single snapshot.
3. Introduction of a new range cell migration correction technique for distributed array echoes, achieving effective range–azimuth decoupling without azimuth signal distortion.

The structure of this paper is organized as follows. Section 2 introduces the geometric configuration and signal model of the distributed array collaborative, forward-looking imaging system. Section 3 elaborates on the proposed image algorithm, incorporating a novel range cell migration correction method, a specific approach for reconstructing gapped azimuth signals, and the subsequent azimuth focusing process. In Section 4, we present and thoroughly discuss the results from both simulation-based and real-data experiments. Section 5 concludes the paper with a summary of our work and key findings.

## 2. Analysis of Geometric Configuration and Signal Model

This section introduces the geometric configuration of the distributed array collaborative imaging system and the transmit–receive signal model. Based on this analysis, the paper elaborates on issues that traditional algorithms fail to address. These primarily include the discontinuity issues in signals from the distributed array and this system's unique range cell migration characteristics.

The geometric configuration of the distributed array collaborative, forward-looking imaging system is depicted in Figure 1. In this arrangement, several aircraft, each equipped with transmit–receive linear arrays, fly in parallel along the X-axis at a constant velocity, $V$. The aircraft maintains a flight altitude of $H$. The central array is designated as the reference array, with the ground projection of its aperture center marked as the origin, $O$. The distributed arrays are aligned along the Y-axis, each characterized by a uniform length, $L$, and inter-array spacing, $D$. In this configuration, the beam center of each array is directed forward and downward, ensuring collective coverage of a common ground area. This setup facilitates collaborative imaging by multiple arrays, enhancing the system's imaging capabilities over the targeted region.

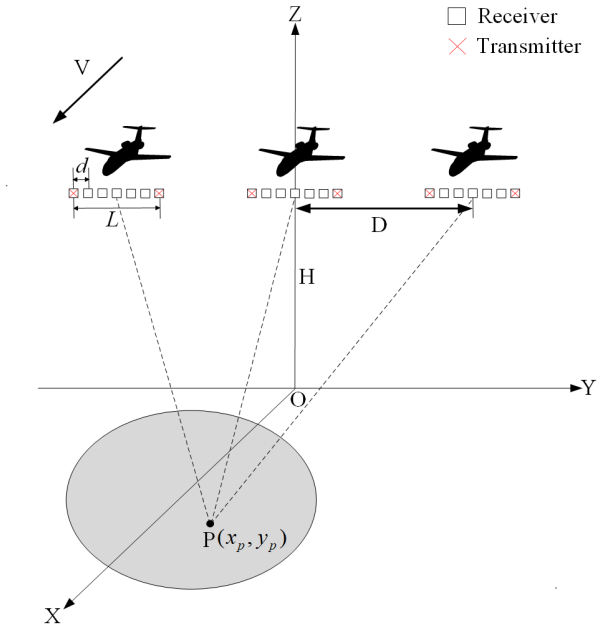



**Figure 1.** Geometric configuration of the system.

### 2.1. Geometric Configuration

In this study, each linear array element adopts a "dual-antenna transmission with N-antenna reception" configuration arranged along the Y-axis. The transmitting antennas are positioned at both ends of the array, while the receiving elements are uniformly distributed along it with an element spacing of $\overline{d}$. The total aperture length of the antenna array is denoted as $L$. Each array independently receives signals it transmits, and multiple arrays achieve signal separation through Time Division Multiplexing (TDM) [45,46]. When the pulse repetition frequency (PRF) is sufficiently high, this arrangement allows for what can be considered simultaneous sampling of the forward-looking region by each array.

The phase center approximation (PCA) method is employed to simplify the complex multi-transmit and multi-receive radar structure [47–49]. By applying appropriate compensations, PCA effectively transforms the MIMO radar's multi-receive–transmit array structure into an equivalent monostatic configuration, where the transmit and receive antennas are assumed to be colocated, as depicted in Figure 2a. This simplified model's effective aperture length remains $L$, and the element spacing is adjusted to $d$. Figure 2b illustrates both the actual configuration of the array and the equivalent virtual array config-

uration achieved through PCA. All subsequent analyses and experiments presented in this paper are based on this simplified configuration.

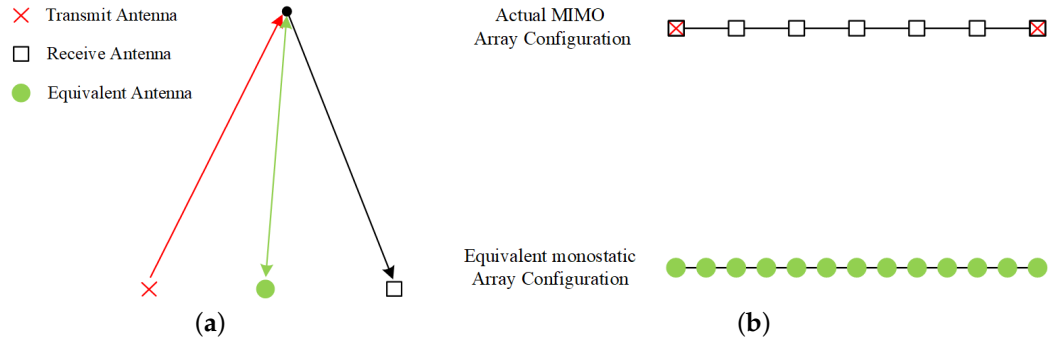



**Figure 2.** Analysis of the single-array configuration. (**a**) Demonstration of equivalent antenna transformation. (**b**) Configuration of actual array and equivalent virtual array.

### *2.2. Signal Model*

The radar system employs the most commonly used linear frequency modulation (LFM) signals in the radar imaging field:

$$s(\hat{t}) = \text{rect}\left(\frac{\hat{t}}{T_p}\right) \cdot \exp\left[j2\pi\left(f_c\hat{t} + \frac{K_r}{2}\hat{t}^2\right)\right] \tag{1}$$

where rect() represents the rectangular window function, $\hat{t}$ indicates the radar's fast time, $f_c$ is the carrier frequency, $T_p$ is the pulse width of the linear frequency modulation signal, and $K_r$ specifies the chirp rate of the LFM signal.

After each array receives the reflected echo from target $P$, the central array is selected as the reference. The echo of the central reference array can be expressed as:

$$\begin{aligned} s_{ref}(\hat{t}, t_m) = \sigma_p \,\text{rect}\left(\frac{t_m}{T_L}\right) \text{rect}\left(\frac{\hat{t} - \frac{2R_p(t_m)}{c}}{T_p}\right) \\ \times \exp\left\{j2\pi\left[f_c(\hat{t} - -\frac{2R_p(t_m)}{c}) + \frac{K_r}{2}(\hat{t} - \frac{2R_p(t_m)}{c})^2\right]\right\} \end{aligned} \tag{2}$$

where $\sigma_p$ represents the echo amplitude related to the target's backscattering coefficient. The variable $t_m$ signifies the equivalent azimuth slow time and the first rectangular window function related to $t_m$ represents the azimuthal element sampling of the central reference array. $T_L$ signifies the array length in terms of azimuth time, satisfying $T_L V_a = L$. Here, $V_a$ is the equivalent azimuth velocity sampled by the system, defined as $V_a/\text{PRI} = d$. Since we convert the model to have each array element sample nearly simultaneously in a single snapshot, the equivalent PRI in the azimuth direction can be arbitrarily set as long as it satisfies the aforementioned equation. To simplify subsequent data processing, we set the equivalent PRI to 1. The variable $c$ denotes the speed of light. The expression $R_p(t_m) = \sqrt{R_{p0}^2 + (V_a t_p)^2}$ calculates the slant range to the target point, where $R_{p0} = \sqrt{x_p^2 + H^2}$ is the shortest perpendicular distance from the target point to the array and $t_p$ represents the azimuth time of the target relative to the center of the reference array.

By setting the azimuth time zero point at the center element of the reference array, it is possible to integrate the sampled echoes from different arrays into a unified echo coordinate system. The gaps in the sampled signals of each array are filled by zero-padding, with the zero-padding length corresponding to the spacing between the arrays. At this point, the sampled signals in the entire coordinate system are coherent. Consequently, the demodulated received echo signal from target $P$ can be expressed as follows:

$$s(\hat{t}, t_m) = \sum_i \sigma_p \operatorname{rect}\left(\frac{t_m - t_{ci}}{T_L}\right) w_r\left(\hat{t} - \frac{2R_p(t_m)}{c}\right) \times \exp\left(-\frac{j4\pi f_c R_p(t_m)}{c}\right) \exp\left[j\pi K_r\left(\hat{t} - \frac{2R_p(t_m)}{c}\right)^2\right] \tag{3}$$

In this formulation, $i$ denotes the index of the distributed arrays, and $t_{ci}$ indicates the center of the $i$-th array at the corresponding slow-time instant, with the relationship $(t_{ci} - t_{ci-1})V_a = D$. For the convenience of expressing the formula, the second rectangular window function, which represents the range direction signal envelope, is replaced with $\omega_r$.

High resolution in the range direction can be achieved through range matching filtering. Following range compression, the signal can be represented as:

$$\begin{aligned} s(\hat{t}, t_m) &= \sum_i \sigma_p \operatorname{rect}\left(\frac{t_m - t_{ci}}{T_L}\right) \operatorname{sinc}\left(\hat{t} - \frac{2R_p(t_m)}{c}\right) \times \exp\left(-j\frac{4\pi f_c R_p(t_m)}{c}\right) \\ &= \sum_i \sigma_p \operatorname{rect}\left(\frac{t_m - t_{ci}}{T_L}\right) \operatorname{sinc}\left(\hat{t} - \frac{2R_p(t_m)}{c}\right) \times \exp\left(-j\frac{4\pi f_c R_{p0}}{c}\right) \\ &\times \exp\left(-j\frac{2\pi V_a^2}{\lambda R_{p0}}(t_m - t_p)^2\right) \end{aligned} \tag{4}$$

For simplicity of expression, in the following sections of this paper, we define $K_a = 2V_a^2/\lambda R_{p0}$ as the equivalent azimuth chirp rate.

### *2.3. Collaborative Processing of Azimuth Signals in Distributed Arrays*

Analysis of Equation (4) reveals that, under the assumption of disregarding range migration, the azimuth signal model corresponds to a discontinuous linear frequency modulated signal. The discontinuities in the signal are determined by the intervals between the arrays. If traditional SAR azimuth focusing techniques are directly applied, the lack of signal periodicity results in cross-modulation artifacts. Such cross-modulation leads to cluttered images with target responses that exhibit significantly high sidelobes. Figure 3 provides a corresponding illustration. In Figure 3a, the envelope of the sampled echo signals from three distributed forward-looking arrays for a central target is shown. The horizontal axis of the image represents the previously mentioned equivalent azimuth slow time. Due to the distributed configuration of the arrays, zero-padding is applied between the sampled signals from different arrays to enable coherent processing. The interval between the array samples is $D/V_a$, and the sampling duration for each array is $T_L$. Figure 3b depicts the azimuth spectrum of the distributed system's echo signals. The horizontal axis represents the equivalent azimuth frequency. Given the linear frequency modulation characteristic of the azimuth signals, there is a certain similarity between the frequency-domain and time-domain modulations. Gaps are also present between the spectra of individual arrays, with the frequency spacing between arrays being $K_a D/V_a$. These gaps lead to cross-modulation of the target response after traditional frequency-domain focusing, as shown in Figure 3c. Specifically, the target response is simultaneously modulated by two sinc functions. The narrower sinc function "spikes" arise from the target response across the total aperture length of all arrays. Due to the distributed array structure, these sharp sinc function spikes are replicated along the azimuth direction, with the envelope formed by a broader sinc function. This broader envelope modulation is attributed to the aperture length of a single array's sampling. Such modulation results in cluttered target responses in the image. The azimuth resolution enhancement is negligible, nearly equivalent to the resolution achieved with single-array imaging. Thus, there is a need for an algorithm that fully leverages the configurational advantages of distributed arrays to focus azimuth signals effectively.

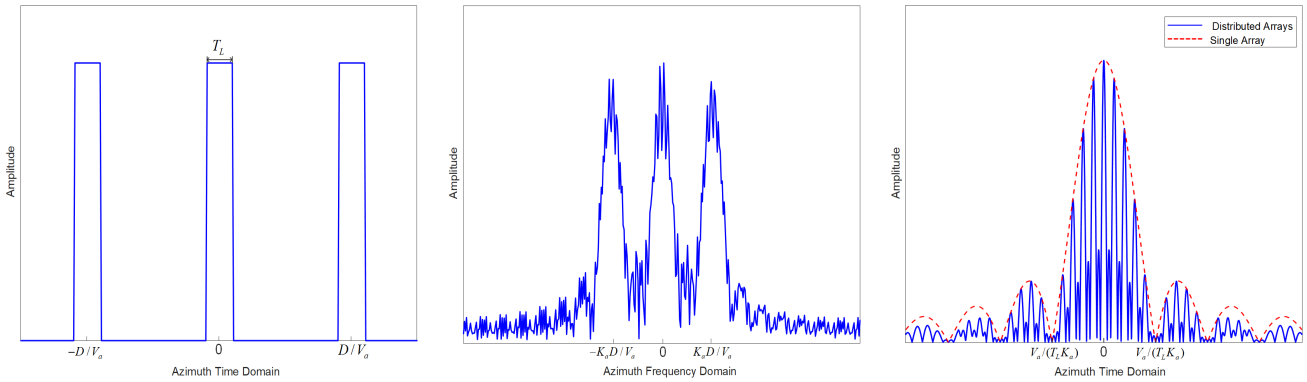



**Figure 3.** Analysis of the mismatch between traditional algorithms and distributed imaging models. (**a**) Azimuth time-domain envelope of echo sampling in distributed arrays. (**b**) Azimuth spectrum of echo sampling in distributed arrays. (**c**) Azimuth focusing results using single-array and distributed multi-array configurations.

### *2.4. Range Cell Migration of Distributed Arrays*

In addition to the challenges of focusing gapped signals, the range cell migration in a distributed collaborative array also differs from traditional scenarios. Two cases are used to analyze the characteristics of range cell migration signals from a distributed system, as depicted in Figure 4: Figure 4a, the single-array condition, and Figure 4b, the multi-array condition.

To analyze the echo signals from a distributed array after range compression, we begin by examining the echoes from a single array. In the range dimension, each target signal compresses into a sinc peak. In the azimuth dimension, the maximum range cell migration for a single array is depicted in Figure 4a and can be expressed as follows:

$$\begin{aligned} |R_2 - R_1| &= \sqrt{{R_{p0}}^2 + \left(L/2 + y_p\right)^2} - \sqrt{{R_{p0}}^2 + \left(L/2 - y_p\right)^2} \\ &= \frac{2y_pL}{\sqrt{{R_{p0}}^2 + \left(L/2 + y_p\right)^2} + \sqrt{{R_{p0}}^2 + \left(L/2 - y_p\right)^2}} \end{aligned} \tag{5}$$

Given that the imaging angle for forward-looking imaging typically does not exceed 20°, and considering $L \ll R_{p0}$ and $L \ll y_p$, we can conclude the following:

$$\begin{aligned} |R_2 - R_1| &= \frac{2y_pL}{\sqrt{{R_{p0}}^2 + \left(L/2 + y_p\right)^2} + \sqrt{{R_{p0}}^2 + \left(L/2 - y_p\right)^2}} \\ &\approx \frac{y_pL}{\sqrt{{R_{p0}}^2 + {y_p}^2}} \leq \frac{R_{p0}\tan 10^\circ L}{\sqrt{{R_{p0}}^2(1 + \tan 10^{\circ 2})}} \approx 0.17L \end{aligned} \tag{6}$$

Due to the aircraft's payload limitations, the aperture length of a single array is generally restricted to less than 3 m. Consequently, the maximum range cell migration, $|R_2 - R_1|$, for a single array relative to target points in the imaging area typically does not exceed 0.5 m. This migration is less than the commonly used range resolution. Therefore, the target echoes from a single array do not cross range cells, eliminating the occurrence of range cell migration.

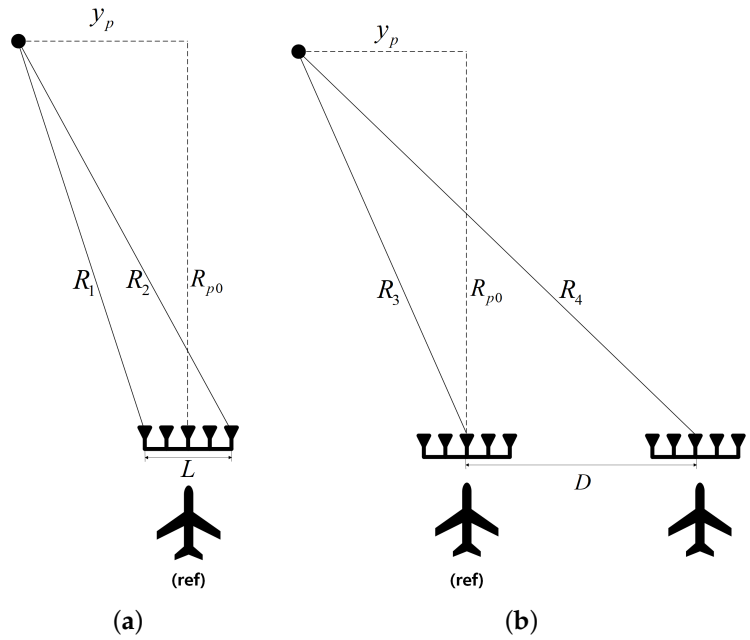



**Figure 4.** Analysis of the system's range cell migration. (**a**) Single-array RCM. (**b**) Inter-array RCM.

In scenarios where multiple arrays are used concurrently to observe an imaging area, maintaining the host aircraft's safety is critical. Consequently, the separation distance, $D$, between arrays is typically set at a minimum of three times the length, $L$, of a single array. For instance, considering the SIREV model that features a single array length of 2.6 m [14], the inter-array distance in such a configuration would be at least 10 m. Under these conditions, the range cell migration, denoted as $|R_3 - R_4|$ and illustrated in Figure 4b, can be quantified as follows:

$$\begin{aligned} |R_3 - R_4| &= \left| \sqrt{{R_{p0}}^2 + {y_p}^2} - \sqrt{{R_{p0}}^2 + \left(D + y_p\right)^2} \right| \\ &= \frac{\left|2y_pD + D^2\right|}{\sqrt{{R_{p0}}^2 + {y_p}^2} + \sqrt{{R_{p0}}^2 + \left(D + y_p\right)^2}} > 3|R_2 - R_1| \end{aligned} \tag{7}$$

According to the formula, it is evident that echoes reflected from targets located at the edges of the imaging area to different arrays may traverse across range cells in the azimuth direction, especially when the distributed system has more than two arrays. Consequently, the range cell migration between arrays becomes significant, necessitating appropriate corrective measures.

## 3. Proposed Imaging Algorithm

Building on the analysis of the signal model and imaging challenges discussed in the previous section, this section will detail the imaging algorithm for the forward-looking model of distributed arrays, divided into three main parts. First, the signals that have undergone range compression are processed with reference range cell migration correction and azimuthal preprocessing to achieve decoupling in both azimuth and range dimensions. Subsequently, using the improved MIAA-AIT algorithm, azimuth signals from the distributed array are extrapolated and interpolated to fill the gaps. Finally, the continuous azimuth signals are focused, and the remaining image distortions are corrected to achieve high-resolution, forward-looking imaging results.

### *3.1. RCMC and Azimuth Preprocessing*

Unlike stripmap mode synthetic aperture radar, where the Doppler histories of echoes from targets within the same range cell but different azimuth cells are identical, the variation

in illumination angles and the constraints imposed by the aperture length cause these histories to differ. Consequently, it is essential in the range-Doppler domain to effectively separate targets located in different azimuth cells for individual correction.

Employing the principle of stationary phase (POSP), we perform an azimuth fast Fourier transform(FFT) on the time-domain signal. This process simplifies the formula, enabling the derivation of the signal form in the range-Doppler domain:

$$\begin{aligned} s(\hat{t}, f_m) = \sum_i \sigma_p \operatorname{sinc}\left(\frac{-f_m/K_a + t_p - t_{ci}}{T_L}\right) \rho_r\left(\hat{t} - \frac{2R_{rd}(f_m)}{c}\right) \\ \times \exp\left(-\frac{j4\pi f_c R_{p0}}{c}\right) \exp\left(j\pi \frac{f_m^2}{K_a}\right) \exp\left(-j2\pi f_m t_p\right) \end{aligned} \tag{8}$$

Analysis of the formula reveals that, in the range-Doppler domain, the spatial separation of the arrays results in a gap in the signal spectrum of the same target, characterized by a discontinuity length of $K_a(D/V_a - T_L)$. It is critical to recognize that, unlike single-array forward-looking imaging, the distributed forward-looking model cannot employ the same range cell migration correction as the stripmap mode. Such an approach would lead to an over-correction of the azimuthal signals of single arrays that do not require correction, resulting in severe spectral leakage and aliasing upon returning to the time domain.

The aforementioned issues arise primarily from two factors. First, the aperture sampling is extremely short relative to the entire imaging area, which causes significant energy leakage in the time domain for the gapped azimuth spectrum after traditional RCMC. Second, the range-variant $K_a$ induces a fan-shaped scaling of the azimuth spectrum along the range direction. Consequently, there is a pressing need for a new azimuth signal alignment algorithm to prevent the failure of coherent synthesis of the final multi-array signals.

To address this issue, this paper introduces a range cell migration correction method designed specifically for batch processing of distributed forward-looking arrays, termed "reference RCMC". This approach is divided into two steps to correct range cell migration effectively.

In the first step, we build upon the previously analyzed conclusion that echo signals from each single array are free from range cell migration effects. By applying minimal range cell migration correction, we align each array's echo, ensuring that the corrected time-domain signals are minimally impacted by the truncation effect of discontinuous signals and the fan-shaped scaling issue in the range-Doppler domain. The specific implementation method is as follows: we use the range cell migration of the reference array echo in the range-Doppler domain as a benchmark, maintaining the reference array echo signal unchanged while adjusting the other array echoes only for their relative differences in range cell migration. This procedure aligns all array echoes to the same range cell as the reference array echo. Since each array echo is affected only by inter-array range cell migration, this step eliminates range and azimuth coupling, while signals from the same target in different arrays achieve azimuth alignment. The required range cell migration correction for non-reference arrays is determined by:

$$\Delta RCM_{\text{ref_i}} = RCM_{\text{i}} - RCM_{\text{ref}} = \frac{\lambda^2 R_{p0}(f_m - K_a t_{ci})^2}{8V_a^2} - \frac{\lambda^2 R_{p0} f_m^2}{8V_a^2} \tag{9}$$

where $\Delta RCM_{\text{ref_i}}$ represents the range cell migration correction for the $i$-th array required in this step, $RCM_{\text{i}}$ represents the overall range cell migration for the $i$-th array at each position within the coordinate system of the reference array, and $RCM_{\text{ref}}$ represents the overall range cell migration for the reference array at the corresponding position. The correction magnitude for the first step of this algorithm, $\Delta RCM_{\text{ref_i}}$, is determined by calculating the difference between $RCM_{\text{i}}$ and $RCM_{\text{ref}}$.

The second step of range cell migration correction is executed subsequent to the completion of azimuth focusing. Any residual range cell migration is regarded as a component

of image distortion at this juncture. Traditional range cell migration correction methods can be employed to address this residual migration within the two-dimensional image domain:

$$\Delta RCM_{\mathrm{rst}} = RCM_{\mathrm{ref}} = \frac{\lambda^2 R_{p0} f_m^2}{8V_a^2} \tag{10}$$

Figure 5 contrasts the first step of the proposed range cell migration correction method with traditional RCMC techniques used in synthetic aperture radar. In Figure 5, a three-array distributed system serves as an example to illustrate RCMC applied to two target signals that share the same minimum slant range and are located at the azimuth center and the edge of the imaging area, respectively. Observations reveal that the traditional method results in some rotation in the azimuth spectrum of the range-Doppler domain, indicative of an overcorrection issue. In the two-dimensional time domain, significant misalignment occurs among target signals from different arrays, with gaps between arrays featuring aliased signals, complicating the coherent integration across array gaps. Conversely, the stepwise RCMC approach utilizes the central array as the reference in the initial step, aligning azimuth target signals effectively. This alignment mitigates overcorrection issues in the azimuth spectrum. Additionally, in the time domain, the absence of aliasing and minimal impact from truncation artifacts are noted in the gaps between arrays. This precise alignment of each target within the range cells corresponding to the slant range of the reference array sets the stage for effective coherent synthesis among arrays.

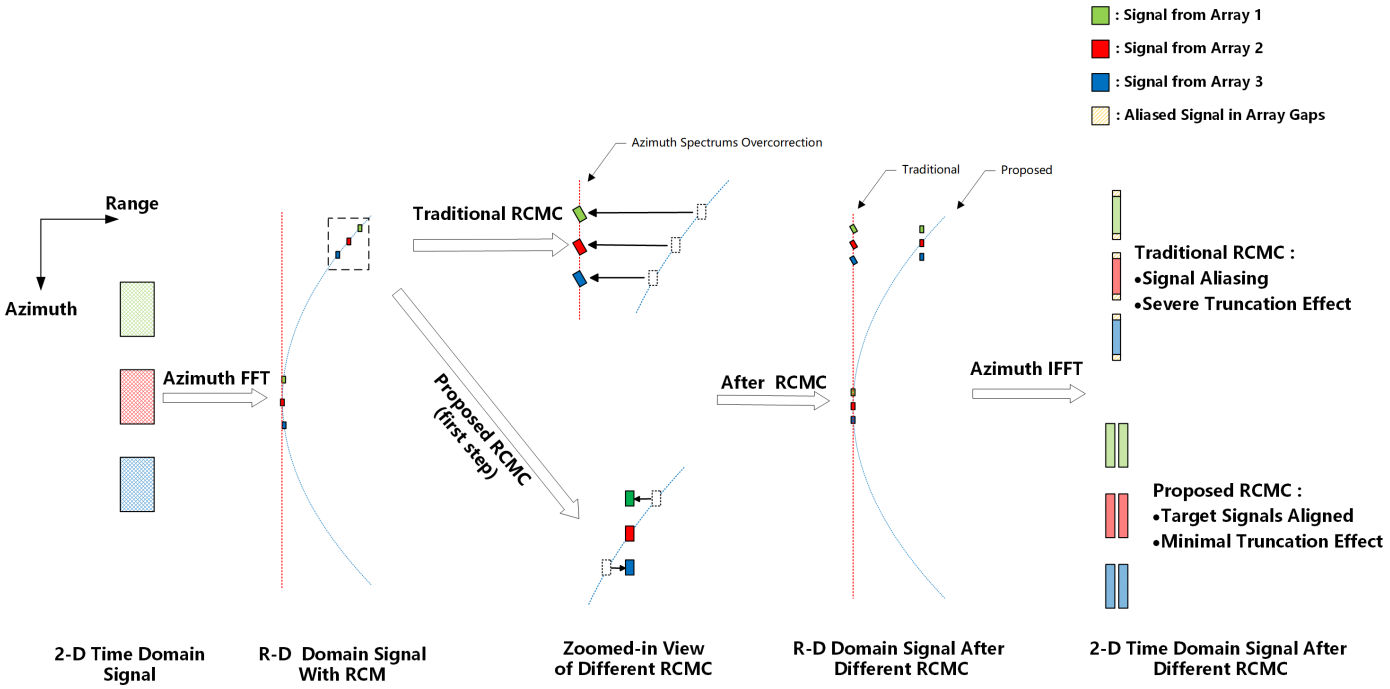



**Figure 5.** Comparison between the proposed RCMC and traditional RCMC.

### *3.2. Recovering Missing Azimuth Signals Using Improved MIAA-AIT*

Upon completing the first step of range cell migration correction, the signal is transformed back into a two-dimensional time-domain representation through an azimuth inverse Fourier transform:

$$\begin{aligned} s(\hat{t}, t_m) = & \sum_i \sigma_p \,\mathrm{rect}\left(\frac{t_m - t_{ci}}{T_L}\right) \rho_r\left(\hat{t} - \frac{2R_{pref}(t_m, i)}{c}\right) \\ & \times \exp\left(-\frac{j4\pi f_c R_{p0}}{c}\right) \exp\left[-j\pi K_a (t_m - t_p)^2\right] \end{aligned} \tag{11}$$

where $R_{pref}(t_m, i) = \sqrt{R_{p0}^2 + V_a^2(t_m - t_{ci} - t_p)^2}$ represents the distance from the reference array to various targets. This formula indicates that, at this stage, the target echoes from different arrays are aligned to the same range cells, facilitating the azimuthal focusing of the signals. It is important to note that, during this phase, each range cell can be isolated for independent subsequent processing. This capability enables the utilization of parallel computing resources such as GPUs, significantly enhancing computational speed.

Due to the spatial separation inherent in distributed arrays, there are extended sampling intervals in the azimuthal domain of the signal. Employing stripmap mode synthetic aperture radar focusing techniques directly on such configurations can induce severe grating lobes during the imaging of targets. While this approach may marginally improve the signal-to-noise ratio of the resultant image, it offers minimal enhancement to actual azimuth resolution, as illustrated in Section 2.3. Consequently, the gaps between array samples are treated as missing signals, which are then predicted and subsequently recovered using available data. Inspired by related algorithms in the ScanSAR domain [50,51], we achieve an azimuth resolution comparable to that of systems with long apertures by integrating virtual and real apertures.

To further refine this solution, we have introduced the iterative adaptive approach (IAA) [52], a robust adaptive parameter estimation method that utilizes the iterative reweighted least squares algorithm to update estimates and filter coefficients continually. This method, superior to other parameter estimation algorithms such as Capon [53] and MUSIC [54], can effectively predict parameters even from a single snapshot. When applied to signals modeled linearly, the IAA can predict and recover missing signals through the missing-data IAA. Unlike aperture interpolation techniques based on the autoregressive Linear Prediction Model (LPM), the MIAA achieves superior data restoration, particularly in conditions where signals are sparse. These capabilities make the MIAA exceptionally well-suited for azimuthal focusing processing in distributed array forward-looking imaging systems.

However, the traditional missing-data iterative adaptive approach cannot be directly applied to forward-looking imaging with distributed arrays without specific modifications and adjustments to the algorithm. A detailed analysis of these necessary changes is provided below and the overall process is illustrated in Figure 6.

The efficacy of the MIAA is contingent upon the sparsity of the signal. In distributed array systems, the azimuth echoes within the Doppler domain often span different subbands for each target, resulting in a relatively dense signal distribution. To address this, it is essential to perform a dechirp process on the azimuth signals of each range cell within the distributed array. This process effectively corrects the spectrum broadening effect of chirp signals, resulting in a more concentrated spectrum, which improves spectral resolution and simplifies subsequent spectral analysis. Following the dechirp, the time-domain signal can be approximated as a superposition of monofrequency signals corresponding to the positions of targets. This approximation facilitates a coarse focusing within the Doppler domain, thus satisfying the sparsity condition required for the MIAA. The specific operations involved are detailed as follows:

The filter signals for the dechirp operation can be represented as follows:

$$h_{\text{dechirp}} = \exp\left(j\pi K_a t_m^2\right) \tag{12}$$

Multiply the azimuth time-domain signals of each range cell by their corresponding filter signals. The resulting dechirped echo signals can be represented as follows:

$$\begin{aligned} s(\hat{t}, t_m) = &\sum_i \sigma_p rect\left(\frac{t_m - t_{ci}}{T_L}\right) \rho_r\left(\hat{t} - \frac{2R_{p_{ref}}(t_m, i)}{c}\right) \\ &\times \exp\left(j2\pi K_a t_p t_m\right) \exp(-j\phi) \end{aligned} \tag{13}$$

where $\phi$ represents the residual fixed phase, which has minimal impact on the overall imaging quality and can thus be disregarded in subsequent processing steps. At this juncture, the echoes from different arrays for the same target are effectively equivalent to single-frequency superimposed signals, albeit with data missing between them. The frequency of these signals corresponds to the target's position. With the preprocessing of the sampled data for the distributed array complete, the relationship between the azimuth signal, $\mathbf{y}$, in each range cell and the coarse focusing result, $\mathbf{r}$, can be expressed as follows:

$$\mathbf{y} = \mathbf{F}\mathbf{r} + \mathbf{n} \tag{14}$$

where $\mathbf{n}$ represents the noise introduced during the observation process. The signal $\mathbf{y}$ comprises the sampled signals from distributed arrays, with each array containing $M$ elements, denoted as $\mathbf{y}_{\text{array}_i} \in \mathbb{C}^{M\times 1}$. Additionally, a zero vector, representing the gaps where signals are missing, is denoted as $\mathbf{y}_{\text{gap}} \in \mathbb{C}^{N_g\times 1}$. Consequently, $\mathbf{y}$ can be expressed as follows:

$$\mathbf{y} = \left[\cdots \mathbf{y}_{\text{array }i-1}, \mathbf{y}_{\text{gap }i-1}, \mathbf{y}_{\text{array }i}, \mathbf{y}_{\text{gap }i}, \mathbf{y}_{\text{array }i+1} \cdots\right]^T \tag{15}$$

$\mathbf{F}$ is the Fourier dictionary matrix, where $\mathbf{F}_i \in \mathbb{C}^{M\times K}$ corresponding to $\mathbf{y}_{\text{array }i}$ can be written as:

$$\mathbf{F}_i = \begin{bmatrix} \mathbf{f}_i(\omega_0) \\ \mathbf{f}_i(\omega_1) \\ \mathbf{f}_i(\omega_2) \\ \vdots \\ \mathbf{f}_i(\omega_{K-1}) \end{bmatrix}^T = \begin{bmatrix} 1 & e^{-j2\pi\frac{t_i}{K}} & e^{-j2\pi\frac{2t_i}{K}} & \cdots & e^{-j2\pi\frac{(K-1)t_i}{K}} \\ 1 & e^{-j2\pi\frac{t_i+1}{K}} & e^{-j2\pi\frac{2(t_i+1)}{K}} & \cdots & e^{-j2\pi\frac{(K-1)(t_i+1)}{K}} \\ 1 & e^{-j2\pi\frac{t_i+2}{K}} & e^{-j2\pi\frac{2(t_i+2)}{K}} & \cdots & e^{-j2\pi\frac{(K-1)(t_i+2)}{K}} \\ \vdots & \vdots & \vdots & \ddots & \vdots \\ 1 & e^{-j2\pi\frac{t_i+T_L-1}{K}} & e^{-j2\pi\frac{2(t_i+T_L-1)}{K}} & \cdots & e^{-j2\pi\frac{(K-1)(t_i+T_L-1)}{K}} \end{bmatrix} \tag{16}$$

where $t_i = t_{c_i} - T_L/2$ and $K$ represents the frequency domain grid. In the MIAA algorithm, $K$ is typically set to be significantly larger than the number of samples, $M$, to meet the prerequisite conditions for sparsity.

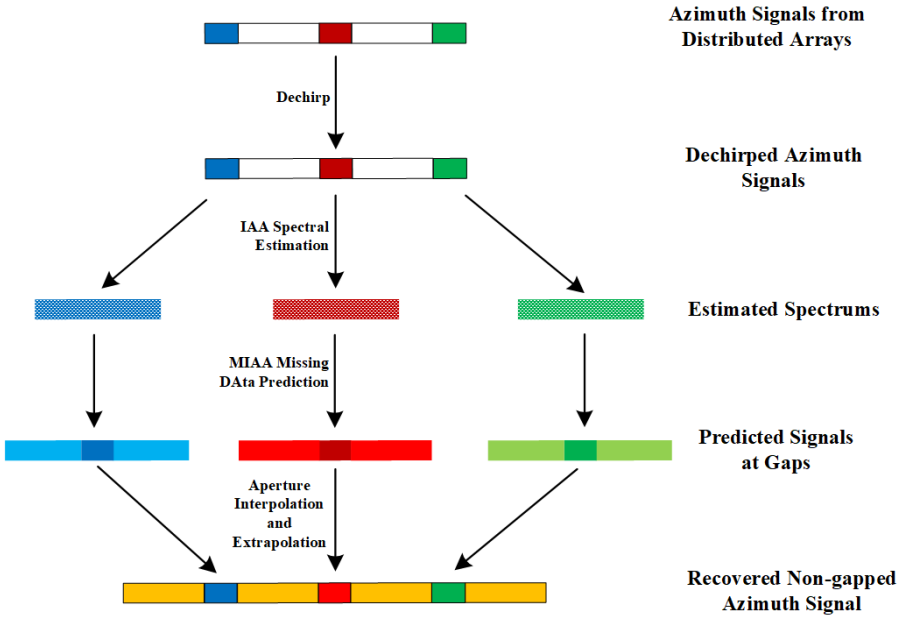



**Figure 6.** Coherent processing of azimuth gapped signals.

Similarly, $\mathbf{F}_{g_i} \in \mathbb{C}^{N_g\times K}$, serving as the Fourier dictionary for the gapped signal between array $i$ and array $i+1$, can be expressed as:

$$\mathbf{F}_{g_i} = \begin{bmatrix} \mathbf{f}_{g_i}(\omega_0) \\ \mathbf{f}_{g_i}(\omega_1) \\ \mathbf{f}_{g_i}(\omega_2) \\ \vdots \\ \mathbf{f}_{g_i}(\omega_{K-1}) \end{bmatrix}^T = \begin{bmatrix} 1 & e^{-j2\pi\frac{t_i+T_L}{K}} & e^{-j2\pi\frac{2(t_i+T_L)}{K}} & \cdots & e^{-j2\pi\frac{(K-1)(t_i+T_L)}{K}} \\ 1 & e^{-j2\pi\frac{t_i+T_L+1}{K}} & e^{-j2\pi\frac{2(t_i+T_L+1)}{K}} & \cdots & e^{-j2\pi\frac{(K-1)(t_i+T_L+1)}{K}} \\ 1 & e^{-j2\pi\frac{t_i+T_L+2}{K}} & e^{-j2\pi\frac{2(t_i+T_L+2)}{K}} & \cdots & e^{-j2\pi\frac{(K-1)(t_i+T_L+2)}{K}} \\ \vdots & \vdots & \vdots & \ddots & \vdots \\ 1 & e^{-j2\pi\frac{t_{i+1}-1}{K}} & e^{-j2\pi\frac{2(t_{i+1}-1)}{K}} & \cdots & e^{-j2\pi\frac{(K-1)(t_{i+1}-1)}{K}} \end{bmatrix} \tag{17}$$

Therefore, our task is to accurately recover the signal **r** for each range cell from the known sparse observation samples, **y**, and the Fourier dictionary, **F**. Typically, various compressed sensing algorithms, such as Orthogonal Matching Pursuit (OMP) [55] and Iterative Shrinkage-Thresholding Algorithm (ISTA) [56], are employed to directly generate estimates of the target distribution, **r**, from the distributed array samples, **y**. This approach is prevalent in applications such as vehicular forward-looking imaging. However, due to various errors, such as jitter introduced during airborne operations, using the overall sampling from distributed arrays to estimate the target distribution can result in significant instability. To address this issue, we note that each subarray has a fixed configuration, resulting in high stability in target parameter estimation. Thus, we first perform signal extrapolation on each array using the MIAA algorithm and then apply aperture interpolation to combine the stable extrapolation results from different arrays.

For the azimuth signal, **y**, of a specific range cell from signal $s(\hat{t}, t_m)$, the initial step is to extract the array signal, $\mathbf{y}_{\text{array}_i}$, from this range cell. Following that, an iterative process based on the IAA method is utilized to obtain a precise estimation of the target's position, **r**. The following are the key steps involved in the MIAA method:

First, obtain the initial estimate of the target spectrum using the periodogram:

$$r_k^{(0)} = \frac{\mathbf{f}_i^H(\omega_k)\mathbf{y}_{\text{array}_i}}{\mathbf{f}_i^H(\omega_k)\mathbf{f}_i(\omega_k)}, \quad k = 0, 1, \ldots, K-1 \tag{18}$$

At the same time, let **P** be a $K \times K$ weight matrix, where the elements $p_k$ correspond to the energy estimates at the frequency grid, $\omega_k$, initialized as $p_k^{(0)} = \left|r_k^{(0)}\right|^2$. Based on this initialization, calculate the covariance matrix $\mathbf{R}_i^{(l+1)}$ of the array signal:

$$\mathbf{R}_i^{(l+1)} = \sum_{k=0}^{K-1} p_k^{(l)} \mathbf{f}_i(\omega_k)\mathbf{f}_i^H(\omega_k) = \mathbf{F}_i\mathbf{P}^{(l)}\mathbf{F}_i^H \tag{19}$$

Here, the superscript $l$ represents the $l$-th iteration. Subsequently, the spectral estimate of the target, $r_k^{(l+1)}$, at each frequency grid point, $\omega_k$, is updated using the covariance matrix.

$$r_k^{(l+1)} = \frac{\mathbf{f}_i^H(\omega_k)(\mathbf{R}_i^{(l+1)})^{-1}\mathbf{y}_{\text{array}_i}}{\mathbf{f}_i^H(\omega_k)(\mathbf{R}_i^{(l+1)})^{-1}\mathbf{f}_i(\omega_k)}, \quad k = 0, 1, \ldots, K-1 \tag{20}$$

Update the diagonal matrix $\mathbf{P}^{(l+1)}$ based on the new spectral estimate of the target **r** and repeat the above iterative process. Typically, around 15 iterations are needed for the final result to converge.

Once precise target estimation results are obtained, employ a linear minimum mean square error (MMSE) estimator to recover the signals in the gaps between $\mathbf{y}_{\text{array}_i}$:

$$\text{argmin}_{\hat{\mathbf{y}}_{\text{gap}_i}} \text{E}\left\{(\hat{\mathbf{y}}_{\text{gap}_i} - \mathbf{T}\mathbf{y}_{\text{array}_i})^H(\hat{\mathbf{y}}_{\text{gap}_i} - \mathbf{T}\mathbf{y}_{\text{array}_i})\right\} \tag{21}$$

where the matrix **T** is the linear transformation estimation matrix for $\hat{\mathbf{y}}_{\text{gap}_i}$ based on $\mathbf{y}_{\text{array}_i}$. By minimizing Equation (21), the estimate of $\hat{\mathbf{y}}_{gap_i}$ is obtained as:

$$\begin{aligned}\hat{\mathbf{y}}_{\text{gap}_i} &= \sum_{k=1}^{K} P_k \mathbf{f}_{g_i}(\omega_k)\mathbf{f}_i^H(\omega_k)\mathbf{R}_i^{-1}\mathbf{y}_{\text{array}_i} \\ &= \sum_{k=1}^{K}\left[P_k \mathbf{f}_i^H(\omega_k)\mathbf{R}_i^{-1}\mathbf{y}_{\text{array}\ i}\right]\mathbf{f}_{g_i}(\omega_k)\end{aligned} \tag{22}$$

It is worth noting that gap $\hat{\mathbf{y}}_{\text{gap}_i}$ can be estimated using forward prediction from $\mathbf{y}_{\text{array}_{i-1}}$ and backward prediction from $\mathbf{y}_{\text{array}_i}$, resulting in different estimates. These diverse prediction results are then coherently combined using aperture interpolation, ultimately yielding the final data estimate for $\hat{\mathbf{y}}_{\text{gap}_i}$.

$$\hat{\mathbf{y}}_{\text{gap}_i}(t_m) = \left(\frac{t_m - t_i}{T_L}\right)\hat{\mathbf{y}}_{\text{gap}_{i-1,i}}(t_m) + \left(\frac{T_L + t_i - t_m}{T_L}\right)\hat{\mathbf{y}}_{\text{gap}_{i,i-1}}(t_m) \tag{23}$$

Traditional MIAA-AIT algorithms only interpolate between array gaps and discard the extrapolation of edge arrays, thereby losing some of the potential virtual apertures, especially when the number of distributed arrays is limited. Therefore, this paper not only performs aperture interpolation within array gaps but also extrapolates the echoes from edge arrays to further extend the virtual aperture. To mitigate issues of divergence that may arise from excessively long extrapolated apertures, the extrapolation length for edge arrays in this study is limited to half of the array gap.

After performing the above operations for all gaps, the array data are restored to a continuous, long-aperture sampled format. The algorithmic flow is summarized in Algorithm 1.

**Algorithm 1**: Implementation of improved MIAA-AIT

**Range cycle:** Traverse all range bin;
**Input:**The azimuthal signal $\mathbf{y}$ ;
**for** each $\mathbf{y}_{\text{array}\ i}$ in $\mathbf{y}$:
**Initialization:**
Target spectrum result vector $\mathbf{r}^{(0)} \in \mathbb{C}^{1\times K}$ with periodogram to $\mathbf{y}_{\text{array}\ i}$:
$r_k^{(0)} = \frac{\mathbf{f}_i^H(\omega_k)\mathbf{y}_{array_i}}{\mathbf{f}_i^H(\omega_k)\mathbf{f}_i(\omega_k)}, \quad k = 0, 1, \ldots, K-1$
Weight diagonal matrix $\mathbf{P}^{(0)} \in \mathbb{C}^{K\times K}$ with the diagonal elements of the $\mathbf{r}^{(0)}$:
$p_k^{(0)} = \left|r_k^{(0)}\right|^2$
**repeat:**
Covariance matrix $\mathbf{R}^{(l+1)}$ update:
$\mathbf{R}_i^{(l+1)} = \sum_{k=0}^{K-1} p_k^{(l)}\mathbf{f}_i(\omega_k)\mathbf{f}_i^H(\omega_k) = \mathbf{F}_i\mathbf{P}^{(l)}\mathbf{F}_i^H$
Target spectrum $r_k^{(l+1)}$ Update:
$r_k^{(l+1)} = \frac{\mathbf{f}_i^H(\omega_k)(\mathbf{R}_i^{(l+1)})^{-1}\mathbf{y}_{\text{array}_i}}{\mathbf{f}_i^H(\omega_k)(\mathbf{R}_i^{(l+1)})^{-1}\mathbf{f}_i(\omega_k)}, \quad k = 0, 1, \ldots, K-1$
Weight Vector $\mathbf{p}^{(l+1)}$ Update: $p_k^{(l+1)} = \left|r_k^{(l+1)}\right|^2$
**until**: convergence or the maximum iterations are reached
**Recover the Gapped Vector Utilizing $\mathbf{y}_{\text{array}\ i}$**
$\mathbf{y}_{\text{gap}\ i} = \sum_{k=1}^{K}\left[p_k\mathbf{f}_i^H(\omega_k)\mathbf{R}_i^{-1}\mathbf{y}_{\text{array}\ i}\right]\mathbf{f}_{g_i}(\omega_k)$
**end for**
**Aperture Interpolation and Extrapolation:** Perform weighted average of all $\mathbf{y}_{\text{gap}}$
**Return:** Non-gapped full-aperture data

### *3.3. Azimuth Focusing and Distortion Correction*

The recovered gap-free, long-aperture sampled signal can be collectively represented as:

$$s(\hat{t}, t_m) = \sum_p \sigma_p \operatorname{rect}\left(\frac{t_m}{T_{L_{total}}}\right) \rho_r\left(\hat{t} - \frac{2R_{p_{ref}}(t_m)}{c}\right) \times \exp(-j2\pi K_a t_p t_m) \exp(-j\Phi) \tag{24}$$

where $T_{L_{total}}$ denotes the total azimuth time span of the entire virtual long aperture. If the aperture signal is directly transformed to the range-Doppler domain for imaging at this stage, the imaging result will exhibit distortions, including fan-shaped distortion and residual range cell migration distortion. Therefore, corresponding corrections are necessary. By performing inverse dechirp operation and zero-padding operations, the signal is restored to the form of the original azimuth chirp signal. At this stage, the signal can be considered equivalent to a long-aperture sampled signal that has undergone range compression and partial range cell migration correction:

$$s_{origin}(\hat{t}, t_m) = s(\hat{t}, t_m) \times \exp\left(-j\pi K_a t_m^2\right) \tag{25}$$

The traditional range-Doppler imaging algorithm's azimuth compression operation is then applied to the signal to achieve azimuth focusing.

$$s_{image}(\hat{t}, t_m) = IFFT_{tm}\left[FFT_{tm}(s_{origin}(\hat{t}, t_m)) \times \exp\left(-j\pi \frac{f_m^2}{K_a}\right)\right] \tag{26}$$

At this stage, the image is focused; however, distortions due to residual range cell migration still require correction. Since the initial step of range cell migration correction involves aligning the azimuth signals of all arrays based on the reference array, the correction for residual range cell migration directly corresponds to the range cell migration of the reference array, as discussed in Section 3.1.

Upon completing the above operations, this method ultimately achieves high-resolution, distortion-free, forward-looking imaging. The overall workflow of the distributed collaborative, forward-looking imaging algorithm proposed in this paper is illustrated in Figure 7. The algorithm process is mainly divided into three parts: range compression and reference RCMC, azimuth gapped data recovery, and azimuth focusing and distortion correction. Taking the example of three arrays, each array first performs independent range compressions. On this basis, the central array is chosen as the reference array, and each array is zero-padded according to its spatial relative position with respect to the reference array, forming a unified coherent coordinate system. Then, the first step of reference range cell migration correction is applied. After this correction, the range-azimuth coupling between arrays is eliminated, allowing for parallel coherent processing of each range cell in the azimuth direction. To begin with, a dechirp preprocessing is conducted, which converts the azimuth signals into a linear superposition of gapped single-frequency signals. Subsequently, the gaps in the signals between arrays are extrapolated and filled using the MIAA algorithm, and the gapped signals are weighted and averaged through aperture interpolation techniques. Afterward, the formed virtual continuous long-aperture signals are restored to their original azimuth signal form via inverse dechirp. At this stage, traditional azimuth focusing can be performed. Once azimuth focusing is completed, the remaining range migration is corrected, ultimately yielding a high-resolution cooperative forward-looking imaging result.

Assume that the distributed array system consists of $M$ arrays, with each array containing $L$ elements. The number of range cells is $N_r$, and the number of azimuth cells is $N_a$. In the MIAA-AIT algorithm, the frequency grid size is denoted as $K$, and the number of iterations is $I$. The following section presents the complexity analysis of the proposed algorithm.

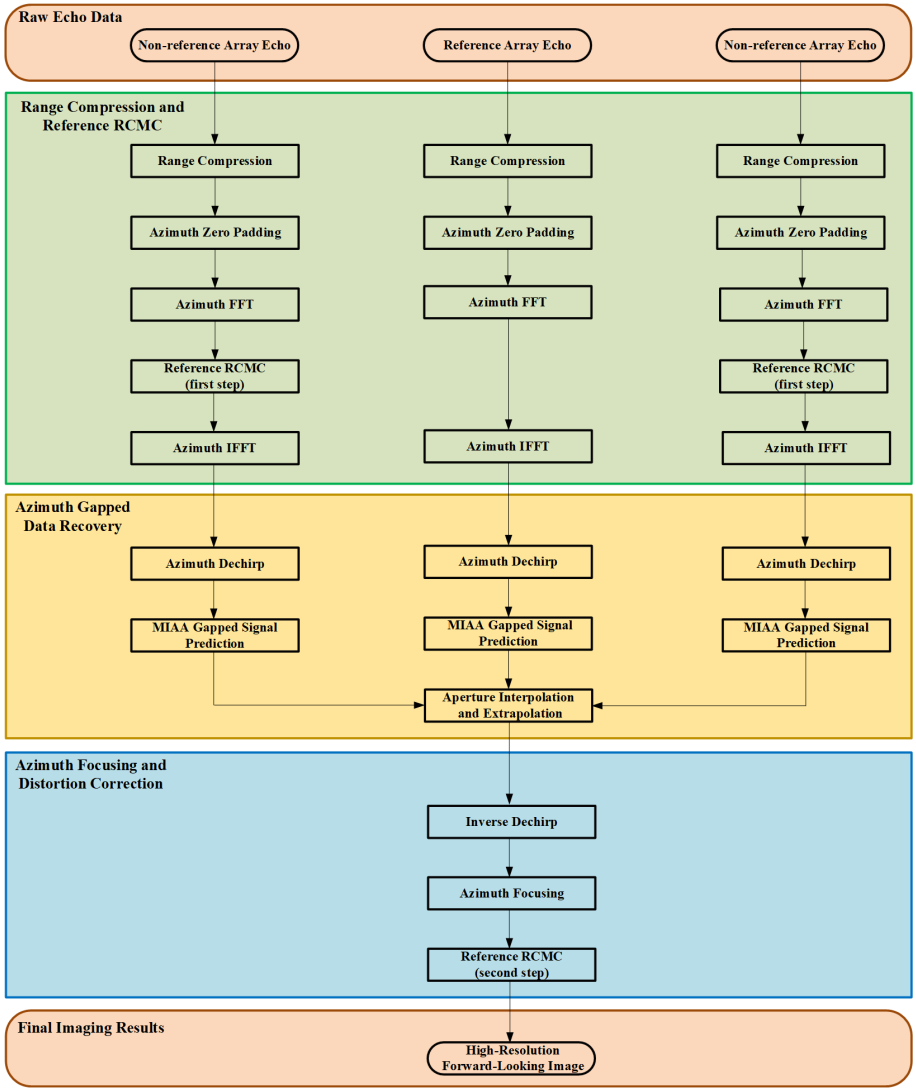



**Figure 7.** Overall workflow of the distributed array collaborative, forward-looking imaging.

For the range compression stage, the distributed system requires $M \times L$ fast Fourier transforms and inverse FFTs of vector size $N_r$, resulting in a complexity of $O(M \cdot L \cdot N_r \cdot \log N_r)$. In the range cell migration correction step, the distributed system requires $M \times N_r$ FFTs and inverse FFTs of vector size $N_a$ for azimuth processing. Additionally, the complexity of the first step of range migration interpolation is $O((M-1) \cdot N_r \cdot N_a)$, while the second step, residual range migration correction, has a complexity of $O(N_r \cdot N_a)$. Therefore, the overall complexity of the range migration process is $O(M \cdot N_r \cdot N_a) + O(N_r \cdot N_a \cdot M \cdot \log N_a)$, which simplifies to $O(N_r \cdot N_a \cdot M \cdot \log N_a)$.

For azimuth dechirping and inverse dechirping, processes have a complexity of $M \cdot N_r \cdot N_a$. In the MIAA-AIT algorithm, gap-filling prediction is required for each range cell and for each array. When the frequency grid size, $K$, is significantly larger than $L$, the complexity of the distributed system's MIAA algorithm is $O(N_r \cdot M \cdot I \cdot K \cdot L^2)$. The subsequent azimuth focusing step requires $N_r$ FFTs and inverse FFTs of vector size $N_a$, resulting in a complexity of $O(N_r \cdot N_a \cdot \log N_a)$.

Therefore, the overall complexity of the proposed forward-looking imaging algorithm is: $O\left(M \cdot N_r\left(L \cdot \log N_r + N_a \cdot \log N_a + I \cdot K \cdot L^2\right)\right)$.

## 4. Results and Discussion

This section validates the effectiveness of the proposed distributed array collaborative forward-looking imaging algorithm, including the reference RCMC technique and the

azimuth signal coherent processing method based on the MIAA-AIT algorithm. The validation is carried out through a series of simulations and experiments, including point target simulations, surface target simulations, and real-world experimental tests, highlighting the algorithm's strong performance in forward-looking imaging.

### *4.1. Point Target Simulation*

This paper first conducts point target simulations and progressively validates the performance of the proposed algorithm in three subsections. Initially, the effectiveness of the newly proposed range cell migration correction algorithm is verified. Next, the validity of the distributed array signal coherent processing based on the MIAA-AIT algorithm is assessed. Building on these results, the imaging performance of distributed coherent array signals processed by various algorithms is compared through simulations.

#### 4.1.1. RCMC Techniques Simulation

To verify the effectiveness of the proposed range cell migration correction method and evaluate its imaging performance across the entire imaging region, 21 point targets were uniformly distributed within the area. The targets were spaced 60 m apart in the range direction and 100 m apart in the azimuth direction, as illustrated in Figure 8.

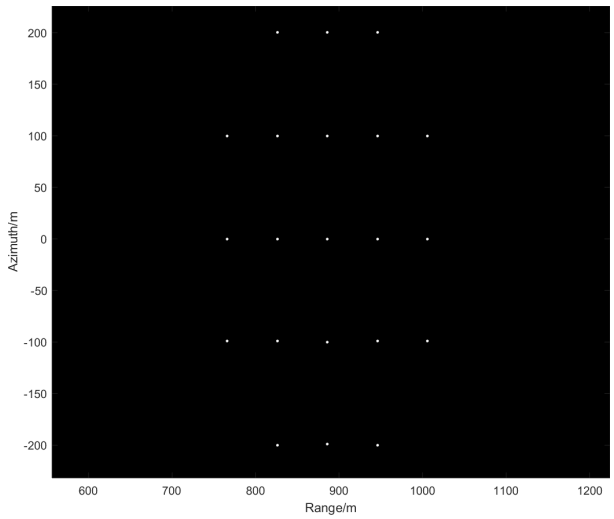



**Figure 8.** Original reference image.

Collaborative imaging was conducted for the designated target area using the distributed imaging model described in this study. The parameters for this imaging model are listed in Table 1.

**Table 1.** Simulation parameters.

| Parameter | Value | Parameter | Value |
|---|---|---|---|
| Center frequency | 9.5 GHz | Element spacing (m) | 0.0471 |
| Bandwidth | 100 MHz | Number of elements | 56 |
| Azimuth beamwidth | 20° | Single aperture length | 2.6387 m |
| Nadir angle | 40° | Array spacing | 10 m |
| Platform height | 1000 m | Number of arrays | 3 |

For the range cell migration correction step, the proposed reference RCMC method and the traditional RCMC method used in conventional SAR were applied separately. After performing range migration correction with each method, coherent processing was carried out using the improved MIAA-AIT algorithm proposed in this paper, leading to the final imaging results. The imaging outcomes were then compared to assess performance.

Figure 9a,b depict the azimuth frequency-domain and time-domain signals of the distributed array after range compression but prior to range migration correction. Figure 9c,d illustrate the azimuth frequency-domain and time-domain signals following traditional SAR RCMC. Figure 9e,f showcase the frequency-domain and time-domain signals after the initial correction step using the proposed reference RCMC. Finally, Figure 9g presents the final imaging results after traditional SAR RCMC, and Figure 9h shows the imaging results from the proposed correction method.

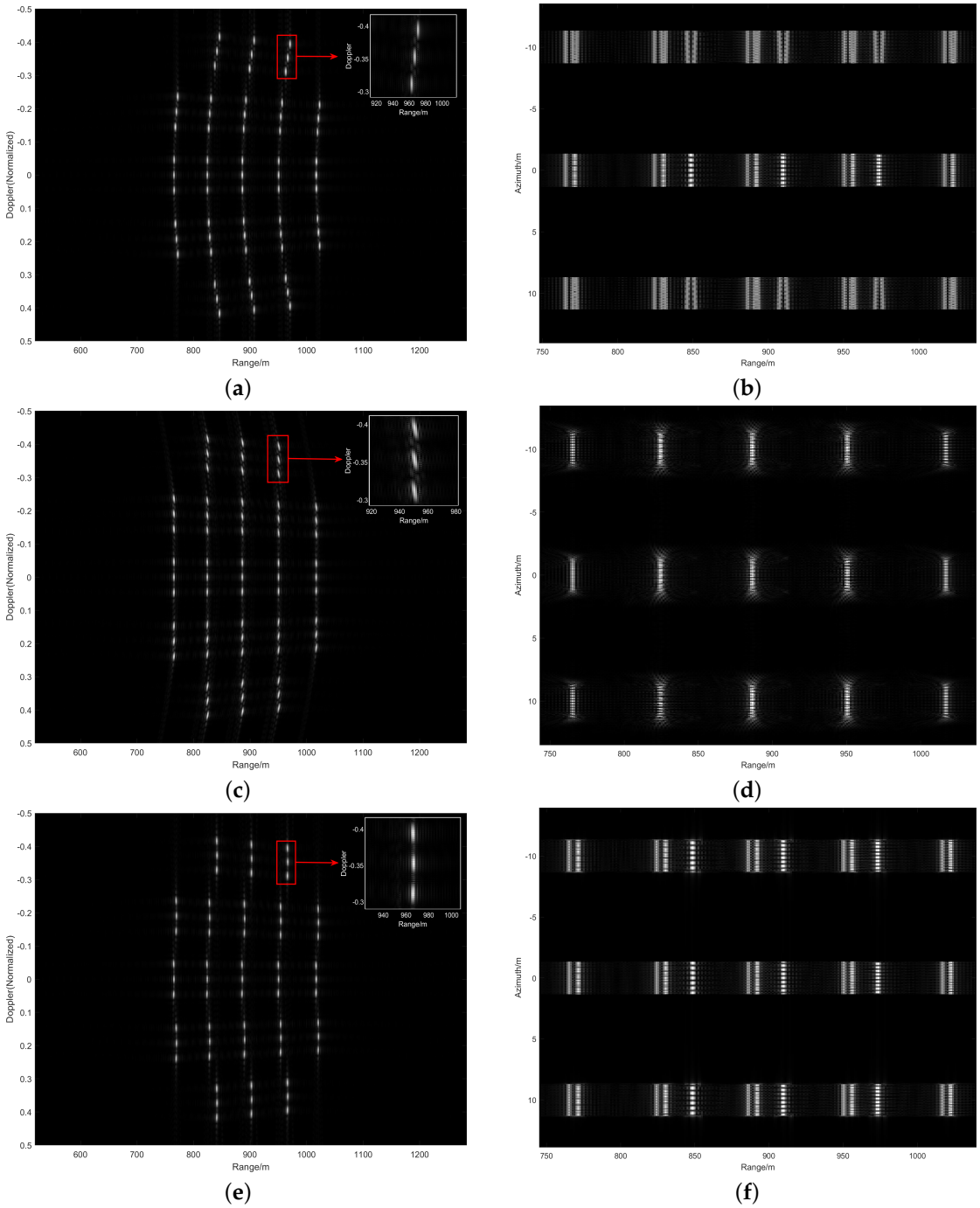



**Figure 9.** *Cont.*

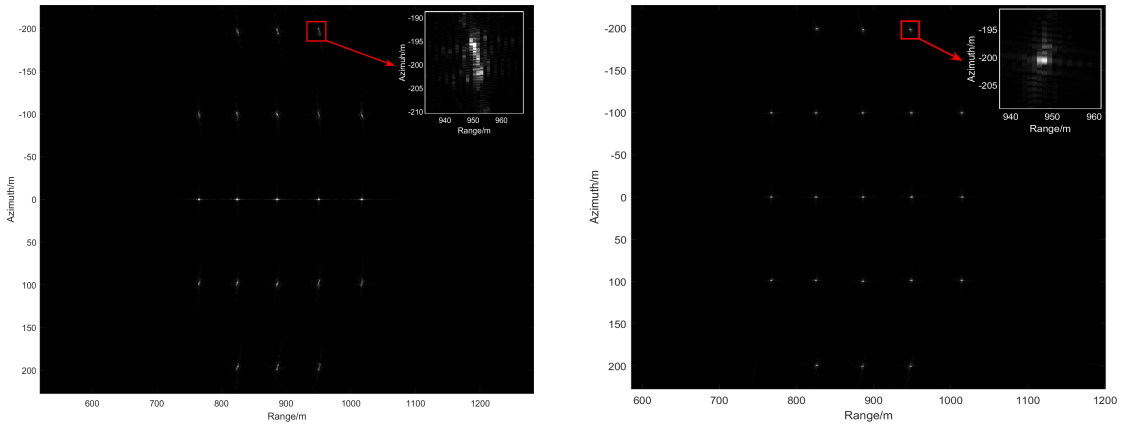



**Figure 9.** Comparative analysis of RCMC algorithms. (**a**) Target signals in the range–Doppler domain before RCMC. (**b**) Target signals in the time domain before RCMC. (**c**) Target signals in the range-Doppler domain after traditional RCMC. (**d**) Target signals in the time domain after traditional RCMC. (**e**) Target signals in the range–Doppler domain after proposed RCMC. (**f**) Target signals in the time domain after proposed RCMC. (**g**) Imaging results using traditional RCMC. (**h**) Imaging results using proposed RCMC.

Experimental results, as shown in the enlarged section of Figure 9a, indicate that, before range correction via RCMC, the azimuth signal spectrum of a single array remains parallel to the azimuth axis and requires no correction. In contrast, the spectra of different arrays span multiple range cells and necessitate corresponding adjustments to align azimuth signals between arrays. Additionally, before any range correction, the time-domain signals of each array remain stable with no energy leakage at the discontinuities between array signals, as depicted in Figure 9b. In an effort to batch-correct range cell migration across arrays, when traditional SAR RCMC methods are employed, the originally parallel target azimuth spectra experience significant rotational skewing, as shown in the enlarged part of Figure 9c. Once reverted to the azimuth time domain, this overcorrection results in displacement and severe truncation effects in the azimuth sampling signals of different arrays, as illustrated in Figure 9d. Such effects lead to a notable widening of the array sampling signals due to the aforementioned overlay, with various extents of target signal shifts across different azimuth positions and even more pronounced signal shifts at the edges of the imaging area. Consequently, this leads to poor recovery of gapped signals in subsequent steps, resulting in suboptimal imaging outcomes, particularly in non-central imaging areas, as can be seen in the magnified diagram of the target at −200 m azimuth distance in Figure 9g, where azimuth resolution deteriorates severely.

In contrast, the stepwise reference RCMC proposed in this paper adjusts only the range cell migration differences relative to the reference array in its first step, thus avoiding the overcorrection issues associated with traditional RCMC, as demonstrated in Figure 9e. Due to the smaller amount of correction, this method minimally disturbs signal amplitude and location, thereby perfectly aligning the target's azimuth signals. When these signals are reverted to the time domain, there are no apparent aliasing or truncation effects, as shown in Figure 9f. This allows for straightforward subsequent operations in gap prediction, achieving excellent overall area imaging results, as shown in Figure 9h. At an azimuth distance of −200 m, the same target, corrected using the proposed reference RCMC method, achieves an enhancement in azimuth resolution comparable to that of the central imaging area targets.

#### 4.1.2. Simulation of the MIAA-AIT-Based Imaging Algorithm for Distributed Array Signals

After applying the reference RCMC, the coupling between the azimuth and range directions of the signal is eliminated, enabling coherent processing of the distributed array's gapped signals. In this section, three point targets, spaced 2.5 m apart along the azimuth direction at the center of the imaging region, are used to compare the resolution performance of the traditional azimuth focusing method with the proposed MIAA-AIT-based discontinuous azimuth signal processing method. Based on this, the imaging performance of the MIAA-AIT algorithm is further evaluated by adjusting the array spacing and signal-to-noise ratio in the distributed array imaging model.

Figure 10a shows the original reference image used for simulations in this section. To clearly compare the imaging performance of different algorithms, a one-dimensional azimuth envelope diagram is used to present the target imaging results, with the actual target positions marked. Figure 10b shows the azimuth envelope of the forward-looking imaging for a single array based on the extended chirp scaling algorithm. Figure 10c presents the target imaging results using the full-aperture processing algorithm based on ECS with three distributed arrays spaced 10 m apart.

Figure 10d shows the time-domain sampled signal of the distributed array, with an array spacing of 10 m and an SNR of 25 dB, after range compression and the first step of reference RCMC. Figure 10e displays the equivalent virtual long-aperture sampled signal formed by applying the MIAA-AIT algorithm, which predicts and fills the gaps in the discontinuous signals and extrapolates the aperture, resulting in a virtual aperture length of approximately 32 m. Figure 10f shows the final coherent imaging results of the distributed array after azimuth focusing. Figure 10g shows the time-domain sampled signal of the distributed array, with an array spacing of 20 m and an SNR of 25 dB, after range compression and reference RCMC. Figure 10h shows the long-aperture signal formed after processing with the MIAA-AIT algorithm, with a virtual aperture length of approximately 52 m. Figure 10i presents the azimuth envelope after subsequent azimuth focusing of the virtual aperture sampled signal. Figure 10j shows the time-domain sampled signal with an array spacing of 10 m and an SNR of 10 dB. Figure 10k shows the long-aperture signal formed after processing with the MIAA-AIT algorithm under these low signal-to-noise ratio conditions, with a virtual aperture length of approximately 32 m. Finally, Figure 10l shows the final target azimuth envelope after further processing of the virtual aperture under low SNR conditions.

In Figure 10b, due to the limited aperture length, the resolution capability of the single-array forward-looking imaging is insufficient, failing to effectively resolve the point targets. In Figure 10c, although three arrays are used for collaborative imaging, the gaps between arrays result in severe sampling modulation. While the signal-to-noise ratio improves under this algorithm, the resolution enhancement is marginal, leaving the targets indistinguishable. In contrast, as shown in Figure 10d–l, the coherent processing of the distributed array using the improved MIAA-AIT algorithm forms a much longer virtual aperture, successfully resolving the targets. By comparing Figure 10f,i, it can be observed that, under high signal-to-noise ratio (SNR) conditions, increasing the array spacing within a certain range leads to an extended virtual aperture length. This results in a narrower target response envelope, thereby improving the resolution performance. Additionally, from the comparison between Figure 10f,l, it is evident that the signal-to-noise ratio has a significant impact on imaging performance; however, even under lower SNR conditions, the distributed array coherent processing based on the MIAA-AIT algorithm can still reliably achieve high-resolution imaging with relative stability.

In the next section, we compared the imaging performance and conducted a statistical analysis of various coherent processing algorithms for discontinuous signals, further validating the superiority of the proposed algorithm.

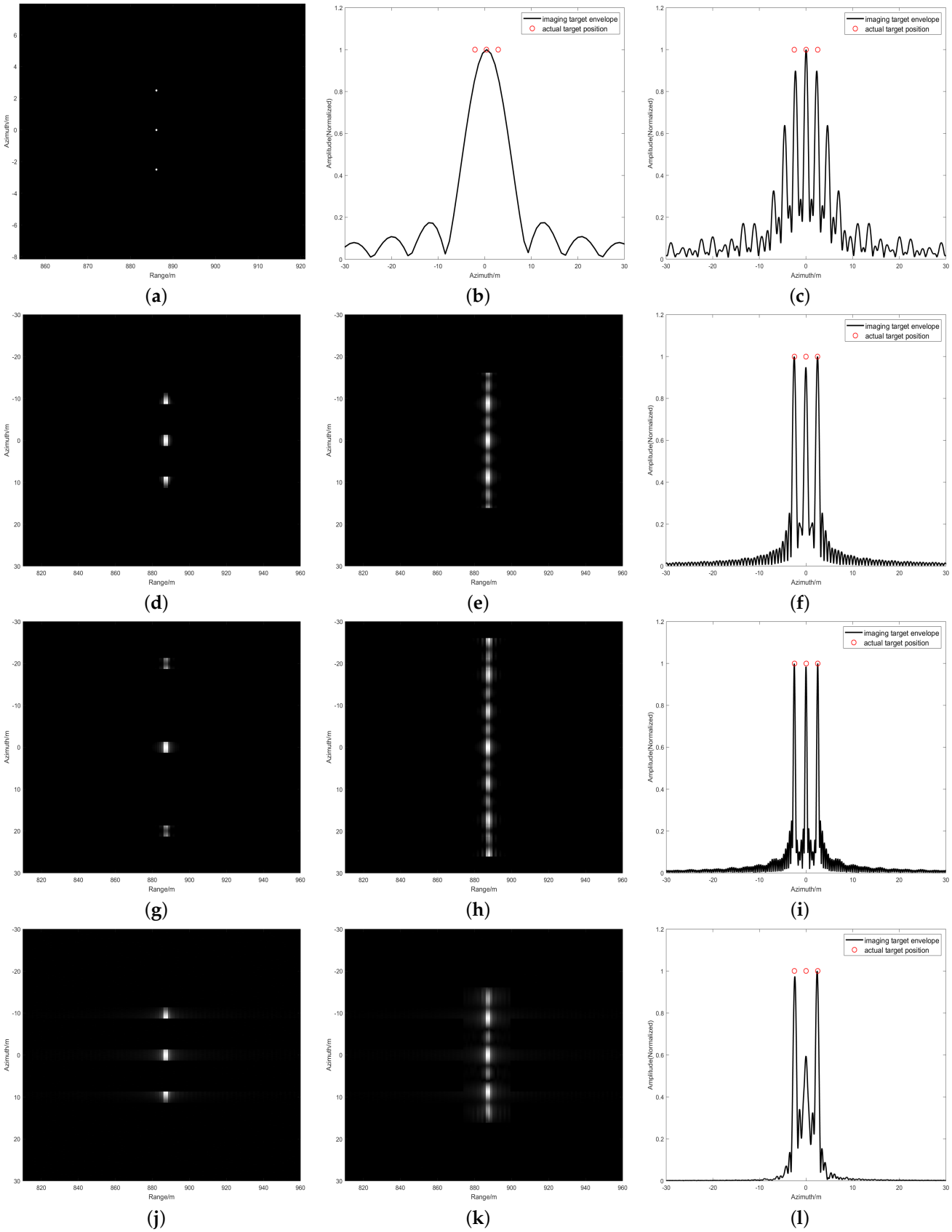



**Figure 10.** Forward−looking imaging performance analysis of the proposed distributed array coherent processing algorithm.(**a**) Original reference image. (**b**) Target envelope formed by ECS using single array. (**c**) Target envelope formed by ECS−based full aperture algorithm. (**d**) Distributed array signals

with an inter−array spacing of 10 m and an SNR of 25 dB. (**e**) Azimuth virtual long−aperture signal formed by the proposed algorithm under the corresponding conditions.(**f**) Target envelope formed by the proposed algorithm under the corresponding conditions. (**g**) Distributed array signals with an inter−array spacing of 20 m and an SNR of 25 dB. (**h**) Azimuth virtual long−aperture signal formed by the proposed algorithm under the corresponding conditions. (**i**) Target envelope formed by the proposed algorithm under the corresponding conditions. (**j**) Distributed array signals with an inter−array spacing of 10 m and an SNR of 10 dB. (**k**) Azimuth virtual long−aperture signal formed by the proposed algorithm under the corresponding conditions. (**l**) Target envelope formed by the proposed algorithm under the corresponding conditions.

#### 4.1.3. Simulation of Various Imaging Algorithms for Distributed Array Signals

Various methods exist for high-resolution imaging of discontinuously sampled signals, which can primarily be categorized into compressive sensing approaches and missing signal prediction recovery methods. This section compares how the imaging performance of different algorithms is affected by aperture sparsity and signal-to-noise ratio variations.

First, we analyze the impact of aperture sparsity on imaging performance across different algorithms, with the SNR set to 25 dB in the following simulations. Since the target amplitudes of the imaging results were normalized in advance, the envelope amplitudes of all targets under each algorithm do not exceed 1. Figure 11a,g show the azimuth envelope of target imaging results using the Linear Prediction Model-AIT algorithm, based on an autoregressive model, with array spacings of 10 m and 20 m, respectively. It can be observed that this signal prediction method struggles to effectively resolve the three targets. In Figure 11g, although three target peaks appear, the two edge targets suffer from severe grating lobes, and their imaging positions are significantly offset from the actual target locations. Figure 11b,h present the azimuth envelope of target imaging results using the GAPES missing signal filling algorithm, based on APES, with array spacings of 10 m and 20 m, respectively. At a spacing of 10 m, this algorithm can clearly resolve the three targets. However, when the array spacing increases to 20 m, resulting in an 82% signal sample missing rate, although three distinct target peaks are still observed, the side targets experience positional shifts, resulting in imaging distortion. Figure 11c,i show the azimuth envelope of target imaging results using the classical Orthogonal Matching Pursuit (OMP) compressive sensing algorithm with array spacings of 10 m and 20 m, respectively. In Figure 11c, while the three targets are resolved, the relative amplitude of the edge targets is low, making them appear as sidelobes of the central target. When aperture sparsity increases further, the OMP algorithm completely fails to resolve the targets. Figure 11d,j show the azimuth envelope of target imaging results using the Iterative Shrinkage Thresholding Algorithm (ISTA) with array spacings of 10 m and 20 m, respectively. At a spacing of 10 m, the targets are clearly resolved. However, when the array spacing increases to 20 m, severe grating lobes appear between the targets, negatively affecting the resolution. Figure 11e,k show the azimuth envelope of target imaging results for single-array forward-looking imaging with real aperture lengths of 20 m and 40 m. The three central targets are distinctly resolved. However, implementing a 20-m-long or even longer airborne array is practically infeasible, as typical forward-looking arrays are no longer than 3 m. In contrast, Figure 11f,l show the azimuth envelope of target imaging results using the proposed improved MIAA-AIT algorithm for forward-looking imaging. The method proposed in this paper achieves imaging quality comparable to that of long-aperture arrays using just three 2.6-m arrays. It successfully resolves the three targets with superior imaging quality and practical feasibility, outperforming other gapped signal processing algorithms. This forward-looking imaging algorithm is particularly effective when the targets are sparsely distributed.

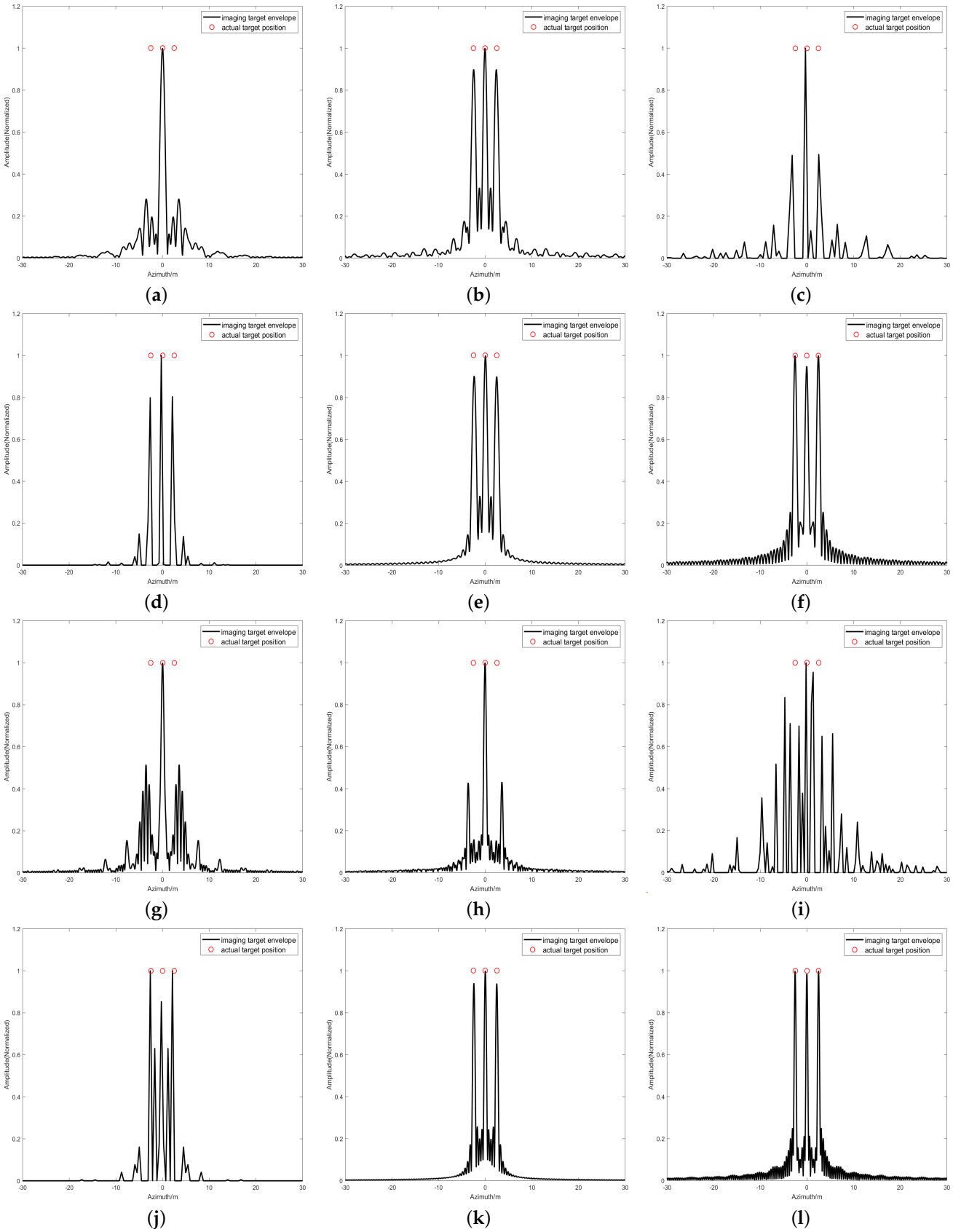



**Figure 11.** Comparative analysis of RCMC algorithms. (**a**) The target envelope based on LPM−AIT with 10 m array spacing. (**b**) The target envelope based on GAPES with 10 m array spacing. (**c**) The

target envelope based on OMP with 10 m array spacing. (**d**) The target envelope based on ISTA with 10 m array spacing. (**e**) Target envelope from ECS algorithm with a 20 m real aperture. (**f**) The target envelope based on improved MIAA−AIT with 20 m array spacing. (**g**) The target envelope based on LPM−AIT with 20 m array spacing. (**h**) The target envelope based on GAPES with 20 m array spacing. (**i**) The target envelope based on OMP with 20 m array spacing. (**j**) The target envelope based on ISTA with 20 m array spacing. (**k**) Target envelope from ECS algorithm with a 40 m real aperture. (**l**) The target envelope based on improved MIAA−AIT with 20 m array spacing.

This paper presents an analysis of the relevant metrics for the point target at the center of the imaging area for each forward-looking imaging model and algorithm, as detailed in Table 2.

To further compare the signal recovery capabilities of different algorithms as aperture sparsity and signal-to-noise ratio vary, we conducted 500 Monte Carlo experiments with different signal missing ratios. The SNRs for these experiments were set to 30 dB, 20 dB, and 10 dB, respectively. The error between the predicted signal and the actual signal was measured using the average mean square error (AMSE), defined as $\mathrm{AMSE}(N_g) = (1/N_g)E\left\{\left\|\mathbf{y}_g - \hat{\mathbf{y}}_g\right\|^2\right\}$ [43].

Figure 12 shows the results. It can be observed that all algorithms experience some impact on their ability to recover missing signals as the SNR decreases. However, in comparison, the MIAA-AIT algorithm demonstrates superior performance in both missing signal recovery and noise resistance compared with other algorithms. Additionally, analysis shows that, for high SNR conditions, the signal missing ratio should be kept below 85% when using the proposed algorithm, while, for lower SNR conditions, the signal missing ratio should be kept below 75%.

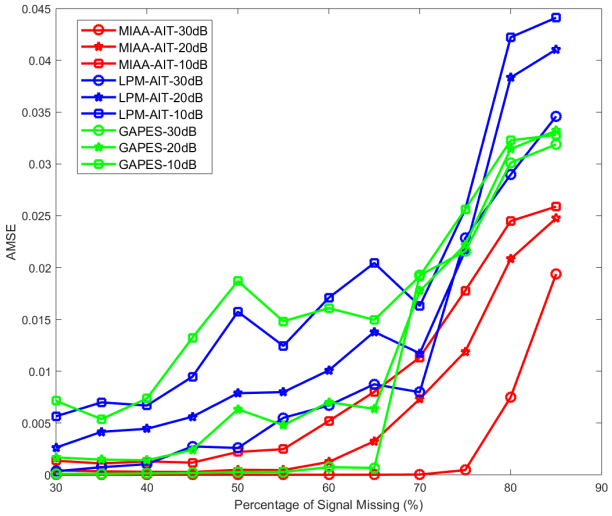



**Figure 12.** Comparison of gapped signal recovery capabilities between different algorithms.

**Table 2.** Point target analysis for each algorithm.

| Imaging Model | Aperture Length/m | Array Spacing/m | Imaging Algorithm | Resolvable | Azimuth Resolution/m | PSLR/dB | ISLR/dB |
|---|---|---|---|---|---|---|---|
| Single array | 2.6 | - | ECS | ✗ | 7.2054 | −13.0125 | −9.9788 |
| Single array | 20 | - | ECS | ✓ | 0.8047 | −13.2821 | −9.8183 |
| Single array | 40 | - | ECS | ✓ | 0.4775 | −13.2613 | −9.8593 |
| Distributed three arrays | 2.6 × 3 | 10 | Full aperture ECS | ✗ | - | - | - |

**Table 2.** *Cont.*

| Imaging Model | Aperture Length/m | Array Spacing/m | Imaging Algorithm | Resolvable | Azimuth Resolution/m | PSLR/dB | ISLR/dB |
|---|---|---|---|---|---|---|---|
| Distributed three arrays | 2.6 × 3 | 10 | LPM-AIT | ✗ | - | – | – |
| Distributed three arrays | 2.6 × 3 | 20 | LPM-AIT | ✗ | - | - | - |
| Distributed three arrays | 2.6 × 3 | 10 | GAPES | ✓ | 0.8408 | −13.0125 | −9.9404 |
| Distributed three arrays | 2.6 × 3 | 20 | GAPES | ✗ | - | - | - |
| Distributed three arrays | 2.6 × 3 | 10 | OMP | ✓ | 0.4315 | −33.2821 | −30.8183 |
| Distributed three arrays | 2.6 × 3 | 20 | OMP | ✗ | - | - | - |
| Distributed three arrays | 2.6 × 3 | 10 | ISTA | ✓ | 0.3518 | −27.1988 | −23.2873 |
| Distributed three arrays | 2.6 × 3 | 20 | ISTA | ✗ | - | - | - |
| Distributed three arrays | 2.6 × 3 | 10 | MIAA-AIT | ✓ | 0.5908 | −12.8999 | −9.6135 |
| Distributed three arrays | 2.6 × 3 | 20 | MIAA-AIT | ✓ | 0.3620 | −12.2282 | −8.7768 |

✗: The three targets are indistinguishable, or the position is significantly offset. ✓: The three targets are clearly distinguishable, with no position offset.

### *4.2. Surface Target Simulation*

To validate the performance of the proposed algorithm in practical environments, this paper presents the simulation results of a distributed forward-looking array targeting surface objects. In all simulations in this section, the signal-to-noise ratio is set to 25 dB. The simulation parameters are detailed in Table 1. The real surface target image used for generating surface target echoes is displayed in Figure 13a. Based on this image, the simulation results are as follows.

The area forward-looking imaging simulation result using a 20 m gapless long-aperture array based on the traditional ECS algorithm is shown in Figure 13b. This result demonstrates effective imaging of the target area, although the image exhibits some scalloping effects that can be corrected in post-processing [57,58]. However, as previously analyzed, achieving such a long aperture length with airborne radar is practically challenging. When using a shorter, more feasible aperture for forward-looking imaging, the azimuth resolution is extremely low, as shown in Figure 13c, making it difficult to resolve the forward-looking area effectively.

On this basis, using a distributed array system significantly improves the forward-looking imaging results compared with a single aperture array. Nevertheless, the results vary with different algorithms. As shown in Figure 13d, the compressed sensing imaging result based on the OMP algorithm compresses each ship target into sparse pixels, leaving only a few strong scatter points on the land, which complicates effective imaging. In contrast, aperture interpolation methods that utilize echo prediction and recovery yield better results.

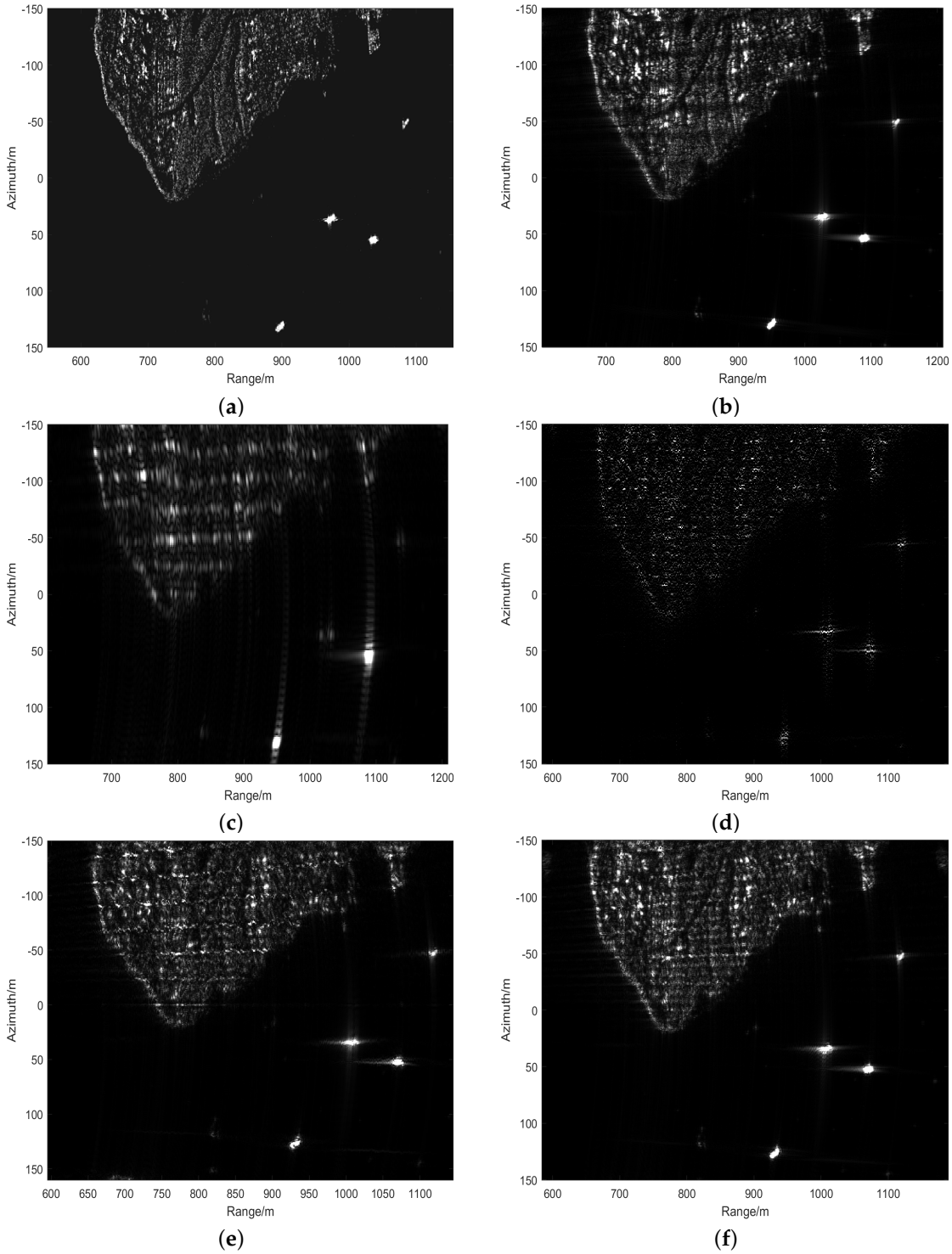



**Figure 13.** Simulation results of surface targets using various algorithms. (**a**) Original image of surface target. (**b**) Imaging results of surface targets using 20 m aperture radar based on ECS algorithm. (**c**) Imaging results of surface targets using single−array radar based on ECS algorithm. (**d**) Imaging results of surface targets using distributed array based on OMP algorithm. (**e**) Imaging results of surface targets using distributed array based on LPM−AIT algorithm. (**f**) Imaging results of surface targets using distributed array based on MIAA−AIT algorithm.

By comparing the imaging results of the ship targets at the bottom of the images and land areas, it can be seen that the imaging result based on the LPM-AIT algorithm, as depicted in Figure 13e, which uses an autoregressive model, exhibits significant disturbances,

with noticeable flickering and jittering of strong scatter points. Conversely, the proposed MIAA-AIT algorithm achieves excellent recovery of the ship targets, and the land targets are clearly distinguishable, realizing a forward-looking imaging performance close to that of the 20 m gapless long-aperture array, as shown in Figure 13f.

### *4.3. Experimental Results with Measured Millimeter-Wave Data*

To assess the performance of the proposed model and its associated algorithm, we conducted forward-looking imaging experiments using a distributed array system based on the AWR2243 cascade radar from Texas Instruments (TI) [59]. The AWR2243 cascade radar supports MIMO mode, enhancing the angular resolution for both medium-range radar (MRR) and short-range radar (SRR) imaging.

When operating in MIMO radar mode, the cascade radar consists of 12 transmit antenna elements and 16 receive antenna elements. According to the principle of equivalent phase centers, the MIMO radar can be equivalently transformed into a SISO mode for each element, resulting in a total of 86 equivalent SISO antenna elements in the azimuth direction, with an equivalent array length of approximately 0.08 m. In this experiment, the AWR2243 cascade radar was used in short-range radar imaging mode, with key parameters listed in Table 3.

**Table 3.** Millimeter-Wave experiment parameters.

| Parameter | Value |
|---|---|
| Center frequency | 78.2 GHz |
| Bandwidth | 2528 MHz |
| Equivalent element spacing | 0.98 mm |
| Number of elements | 86 |
| Equivalent single array aperture length | 8.4 cm |
| Radar-to-target distance | 7.1 m |
| Rail length | 0.5 m |

The experimental setup is illustrated in Figure 14a,b. To achieve distributed imaging, a high-precision rail with a length of 0.5 m was used to move the AWR2243 cascade radar to different positions for sampling. This setup effectively simulates a distributed array forward-looking imaging model. The primary setup in this experiment confirmed the imaging efficacy with an array spacing quintuple that of the aperture length, approximately 0.42 m, and a signal missing rate exceeding 65%. The imaging targets consisted of four corner reflectors positioned at 7.1 m and 8.7 m, with a 0.1-m separation between reflectors 1 and 3.

The experimental results are as follows. Figure 14c,d shows the imaging result generated by sampling each position along the rail, creating a 0.5-m-long array signal. The zoomed-in image of Figure 14c and the three target envelopes in Figure 14d reveal that each corner reflector at 7.1 m can be clearly resolved, with a resolution of 0.0314 m for reflector 2, as detailed in Table 4. Conversely, employing a single array for forward-looking imaging, as illustrated in Figure 14e,f, results in indistinguishable and overlapping targets, rendering their resolution unfeasible.

To address this, we applied an equivalent distributed array model, utilizing rail movements to image the target area using various algorithms, as depicted in Figure 14g–p. All gapped signal recovery algorithms successfully resolved the three corner reflectors. However, due to the sensitivity of the compressed sensing algorithm to noise, the imaging results of the OMP- and ISTA-based algorithms exhibit sidelobes, making it difficult to clearly distinguish the three targets, as shown in Figure 14g–i.

In the imaging experiment using the LPM-AIT algorithm (Figure 14k,l), although the corner reflectors were discernible, signal recovery was compromised by gaps exceeding 65%, leading to a reduced azimuth resolution of approximately 0.0925 m. The target imaging performance based on GAPES was superior to that of LPM-AIT, as shown in

Figure 14m,n. Its resolution was better, about 0.0671 m, but the envelope of the reflector target located at the center was still relatively wide compared with the full aperture. In contrast, the proposed MIAA-AIT algorithm achieved clear and distinguishable imaging of the three targets, with an azimuth resolution of 0.0328 m and no grating lobe interference, as shown in Figure 14o,p and Table 4. The imaging result was comparable to that of full-aperture imaging and superior to the other methods.

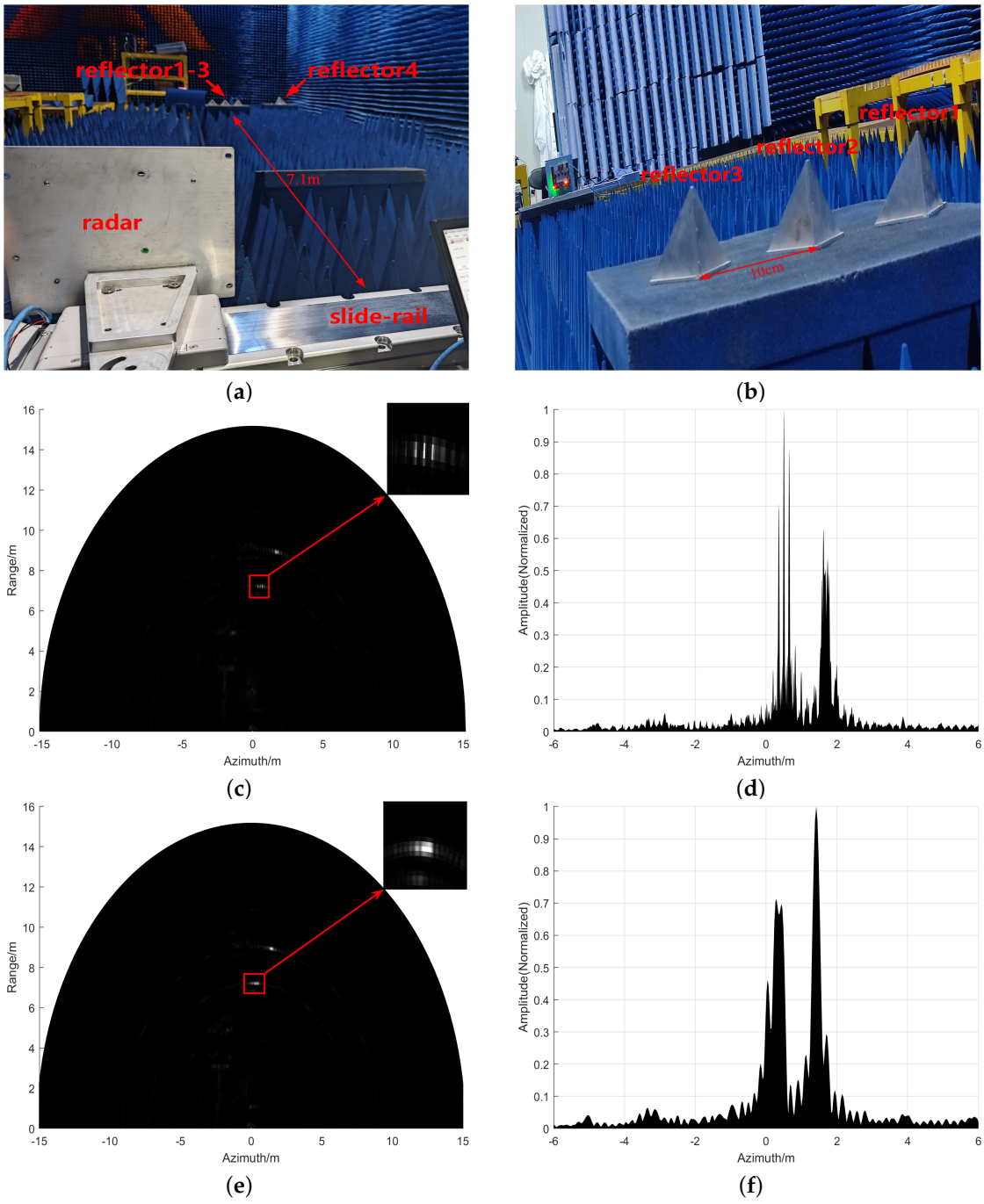



**Figure 14.** *Cont.*

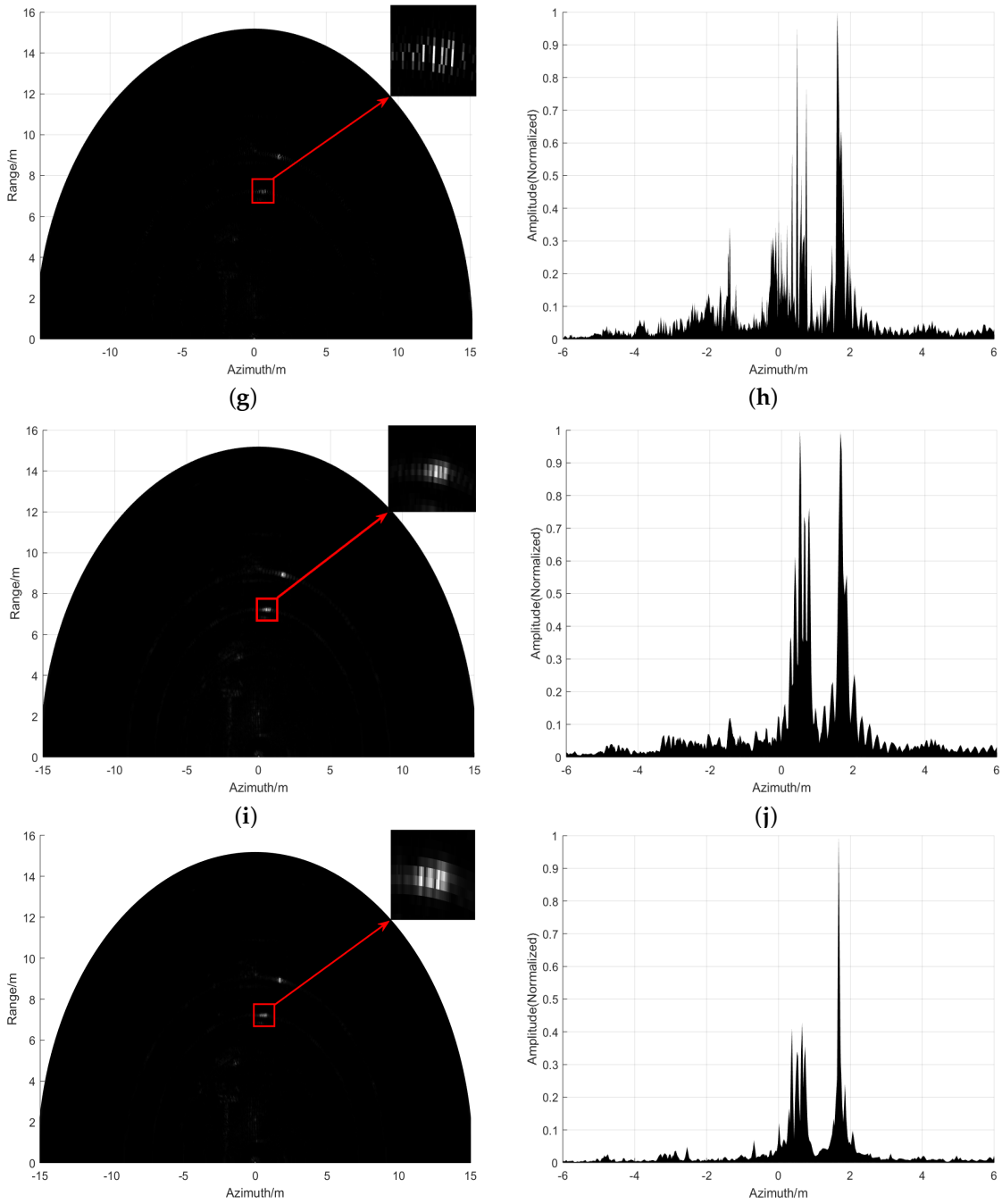



**Figure 14.** *Cont.*

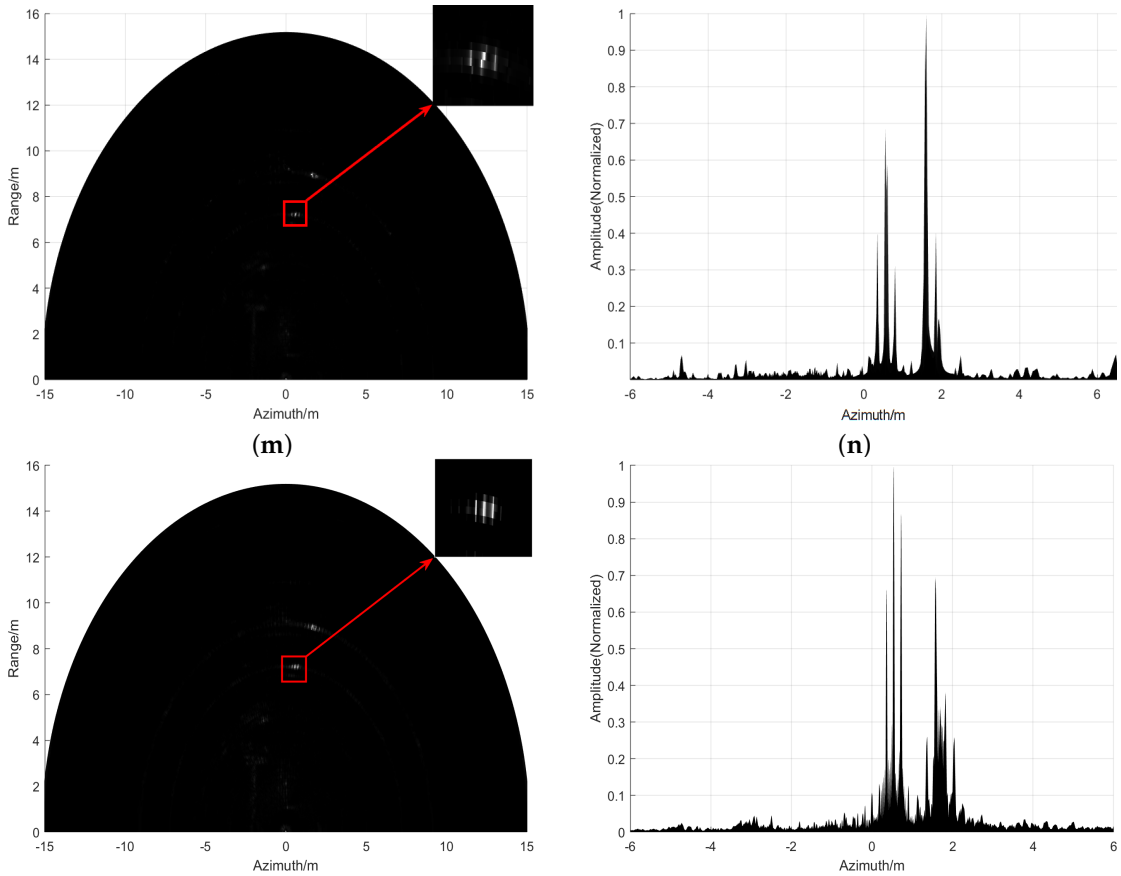



**Figure 14.** Comparison of algorithms with measured data (**a**) Overall experimental setup photo1. (**b**) Overall experimental setup photo2. (**c**) Imaging results with 0.5 m synthetic array. (**d**) Target azimuth envelope imaging results with 0.5 m synthetic array. (**e**) Imaging results with single cascade radar. (**f**) Target azimuth envelope imaging results with single cascade radar. (**g**) Imaging results using distributed array based on OMP algorithm. (**h**) Target azimuth envelope imaging results using distributed array based on OMP algorithm. (**i**) Imaging results using distributed array based on ISTA algorithm. (**j**) Target azimuth envelope imaging results using distributed array based on ISTA algorithm. (**k**) Imaging results using distributed array based on LPM−AIT algorithm. (**l**) Target azimuth envelope imaging results using distributed array based on LPM−AIT algorithm. (**m**) Imaging results using distributed array based on GAPES algorithm. (**n**) Target azimuth envelope imaging results using distributed array based on GAPES algorithm. (**o**) Imaging results using distributed array based on MIAA−AIT algorithm. (**p**) Target azimuth envelope imaging results using distributed array based on MIAA−AIT algorithm.

**Table 4.** Reflector target analysis for each algorithm.

| Imaging Model | Aperture Length/m | Imaging Algorithm | Resolvable | Azimuth Resolution/m | PSLR/dB | ISLR/dB |
|---|---|---|---|---|---|---|
| Single array | 0.084 | Beamforming | ✗ | $\geq$0.10 | - | - |
| Synthetic array | 0.42 | Beamforming | ✓ | 0.0314 | −13.4881 | −13.4632 |
| Distributed two arrays | 0.084 × 2 | OMP | ✗ | - | - | - |
| Distributed two arrays | 0.084 × 2 | ISTA | ✗ | - | - | - |
| Distributed two arrays | 0.084 × 2 | LPM-AIT | ✓ | 0.0925 | −13.2821 | −9.8183 |
| Distributed two arrays | 0.084 × 2 | GAPES | ✓ | 0.0671 | −11.7116 | −8.2385 |
| Distributed two arrays | 0.084 × 2 | MIAA-AIT | ✓ | 0.0328 | −10.6285 | −9.5112 |

✗: The three targets are indistinguishable. ✓: The three targets are clearly distinguishable.

## 5. Conclusions

Aperture length significantly impacts the performance of airborne forward-looking imaging. However, platform payload constraints make achieving a sufficiently long azimuth aperture with a single airborne platform challenging. To overcome this limitation, we introduce a novel distributed MIMO radar forward-looking imaging method, employing multiple aircraft equipped with linear arrays for coherent imaging. In the corresponding forward-looking algorithm, the distributed array sampling signals are treated as a signal missing model. Utilizing the improved MIAA-AIT algorithm, the discontinuous radar array signals are reconstructed into a virtual gapless long array signal. Furthermore, the proposed reference RCMC method, through step-by-step correction, achieves two-dimensional decoupling of radar signals and effectively reduces signal aliasing compared with traditional RCMC techniques. Extensive simulation and experimental data have substantiated that this method can stably and effectively realize high-resolution forward-looking imaging with a single snapshot, achieving imaging performance comparable to that of a long array. The research demonstrates notable advantages, considerably broadening the research horizons in the field of airborne radar forward-looking imaging. For future research, we will focus on the motion compensation algorithms for spatially distributed arrays, as well as time, frequency, and phase synchronization compensation between arrays, in order to achieve stable, high-resolution forward-looking imaging.

**Author Contributions:** Conceptualization, S.S., X.N. and S.H.; methodology, S.S.; software, Z.Z.; validation, S.S., Z.Z. and S.H.; formal analysis, S.S.; investigation, S.S.; resources, X.N., J.G. and S.H.; writing—original draft preparation, S.S.; writing—review and editing, S.H.; supervision, S.H. All authors have read and agreed to the published version of the manuscript.

**Funding:** This research was funded by The National Ministries Foundation of grant number 22-TQ03-01-ZT-01-012.

**Informed Consent Statement:** Not applicable.

**Data Availability Statement:** Data are contained within the article.

**Conflicts of Interest:** The authors declare no conflicts of interest.

## References

1. Yang, R.; Li, H.; Li, S.; Zhang, P.; Tan, L.; Gao, X.; Kang, X. *High-Resolution Microwave Imaging*; Springer: Cham, Switzerland, 2018.
2. Baizert, P.; Hale, T.B.; Temple, M.A.; Wicks, M.C. Forward-looking radar GMTI benefits using a linear frequency diverse array. *Electron. Lett.* **2006**, *42*, 1311–1312. [CrossRef]
3. Li, W.; Chen, R.; Yang, J.; Wu, J.; Huang, Y. Multichannel Radar Forward-Looking Imaging: Potential and Challenges. In Proceedings of the IGARSS 2023—2023 IEEE International Geoscience and Remote Sensing Symposium, Pasadena, CA, USA, 16–21 July 2023; IEEE: New York, NY, USA, 2023; pp. 8273–8276. [CrossRef]
4. Lu, J.; Zhang, L.; Wei, S.; Li, Y. Resolution enhancement for forwarding looking multi-channel SAR imagery with exploiting space–time sparsity. *IEEE Trans. Geosci. Remote Sens.* **2022**, *61*, 5200617. [CrossRef]
5. Zheng, Z.; Tan, G.; Jiang, D. A Bidirectional Resampling Imaging Algorithm for High Maneuvering Bistatic Forward-Looking SAR Based on Chebyshev Orthogonal Decomposition. *IEEE Trans. Geosci. Remote Sens.* **2024**, *62*, 5211512. [CrossRef]
6. Zhong, T.; Tao, H.; Cao, H.; Liao, H. Multiparameter Estimation for Monostatic FDA-MIMO Radar with Polarimetric Antenna. *IEEE Trans. Antennas Propag.* **2024**, *72*, 2524–2539. [CrossRef]
7. Chen, X.; Dong, Z.; Zhang, Z.; Tu, C.; Yi, T.; He, Z. Very High Resolution Synthetic Aperture Radar Systems and Imaging: A Review. *IEEE J. Sel. Top. Appl. Earth Obs. Remote Sens.* **2024**, *17*, 7104–7123. [CrossRef]
8. Kumar, S.A.; G, A.; S, V.G.; Srihari, P.; Pardhasaradhi, B.; Cenkeramaddi, L.R. Real-time Radar Imaging with Time Domain Correlation and Doppler Beam Sharpening. In Proceedings of the 2024 IEEE International Conference on Electronics, Computing and Communication Technologies (CONECCT), Bangalore, India, 12–14 July 2024; pp. 1–6. [CrossRef]
9. Yang, H.; Mao, D.; Zhang, Y.; Zhang, Y.; Huang, Y.; Yang, J. Doppler beam sharpening imaging based on fast iterative adaptive approach. In Proceedings of the 2017 IEEE Radar Conference (RadarConf), Seattle, WA, USA, 8–12 May 2017; IEEE: New York, NY, USA, 2017; pp. 1419–1423. [CrossRef]
10. Lu, J.; Wang, X.; Cao, Y.; Zhang, L. Sparsity-Based Joint Array Calibration and Ambiguity Resolving for Forward-Looking Multi-Channel SAR Imagery. *Remote Sens.* **2023**, *15*, 647. [CrossRef]

11. Zhang, X.; He, M.; He, Z.; Hongyan, S.; Zhang, J. Research on mono-pulse forward-looking imaging airborne radar system. In Proceedings of the IET Conference Proceedings, Xi'an, China, 14–16 April 2013; The Institution of Engineering & Technology: London, UK, 2013. [CrossRef]
12. Alland, S. Antenna requirements and architecture tradeoffs for an automotive forward looking radar. In Proceedings of the 1998 IEEE Radar Conference, RADARCON'98. Challenges in Radar Systems and Solutions (Cat. No.98CH36197), Dallas, TX, USA, 4 May 1998; pp. 367–372. [CrossRef]
13. Mittermayer, J.; Wendler, M.; Krieger, G.; Sutor, T.; Moreira, A.; Buckreuss, S. Sector imaging radar for enhanced vision (SIREV): Simulation and processing techniques. In Proceedings of the Enhanced and Synthetic Vision 2000, Orlando, FL, USA, 24–28 April 2000; SPIE: Bellingham, WA, USA, 2000; Volume 4023, pp. 298–305. [CrossRef]
14. Krieger, G.; Mittermayer, J.; Buckreuss, S.; Wendler, M.; Sutor, T.; Witte, F.; Moreira, A. Sector imaging radar for enhanced vision. *Aerosp. Sci. Technol.* **2003**, *7*, 147–158. [CrossRef]
15. Lu, J.; Zhang, L.; Quan, Y.; Meng, Z.; Cao, Y. Parametric Azimuth-Variant Motion Compensation for Forward-Looking Multichannel SAR Imagery. *IEEE Trans. Geosci. Remote Sens.* **2021**, *59*, 8521–8537. [CrossRef]
16. Qian, G.; Wang, Y.; Zhang, B.; Liu, M. Bistatic Forward-Looking SAR Imaging of Uniformly Moving Target Based on Improved BP Algorithm. *IEEE Trans. Comput. Imaging* **2023**, *9*, 1006–1017. [CrossRef]
17. Li, Y.; Zhang, T.; Mei, H.; Quan, Y.; Xing, M. Focusing Translational-Variant Bistatic Forward- Looking SAR Data Using the Modified Omega-K Algorithm. *IEEE Trans. Geosci. Remote Sens.* **2022**, *60*, 5203916. [CrossRef]
18. Li, Y.; Xu, G.; Zhou, S.; Xing, M.; Song, X. A Novel CFFBP Algorithm With Noninterpolation Image Merging for Bistatic Forward-Looking SAR Focusing. *IEEE Trans. Geosci. Remote Sens.* **2022**, *60*, 5225916. [CrossRef]
19. Qian, G.; Wang, Y. Analysis of Modeling and 2-D Resolution of Satellite–Missile Borne Bistatic Forward-Looking SAR. *IEEE Trans. Geosci. Remote Sens.* **2023**, *61*, 5222314. [CrossRef]
20. Mao, D.; Tuo, X.; Luo, J.; Zhang, P.; Zhang, Y.; Zhang, Y.; Huang, Y.; Yang, J. Scanning Radar Forward-Looking Imaging Under High-Speed Platform by Accurate Profile-Phase Deconvolution Method. *IEEE Trans. Geosci. Remote Sens.* **2024**, *62*, 5107613. [CrossRef]
21. Huo, W.; Tuo, X.; Zhang, Y.; Zhang, Y.; Huang, Y. Balanced Tikhonov and Total Variation Deconvolution Approach for Radar Forward-Looking Super-Resolution Imaging. *IEEE Geosci. Remote Sens. Lett.* **2022**, *19*, 3505805. [CrossRef]
22. Tan, K.; Lu, X.; Yang, J.; Su, W.; Gu, H. A novel Bayesian super-resolution method for radar forward-looking imaging based on Markov random field model. *Remote Sens.* **2021**, *13*, 4115. [CrossRef]
23. Chen, H.; Li, Y.; Gao, W.; Zhang, W.; Sun, H.; Guo, L.; Yu, J. Bayesian Forward-Looking Superresolution Imaging Using Doppler Deconvolution in Expanded Beam Space for High-Speed Platform. *IEEE Trans. Geosci. Remote Sens.* **2022**, *60*, 5105113. [CrossRef]
24. Han, J.; Zhang, S.; Zheng, S.; Wang, M.; Ding, H.; Yan, Q. Bias Analysis and Correction for Ill-Posed Inversion Problem with Sparsity Regularization Based on L 1 Norm for Azimuth Super-Resolution of Radar Forward-Looking Imaging. *Remote Sens.* **2022**, *14*, 5792. [CrossRef]
25. Li, W.; Niu, M.; Zhang, Y.; Huang, Y.; Yang, J. Forward-Looking Scanning Radar Superresolution Imaging Based on Second-Order Accelerated Iterative Shrinkage-Thresholding Algorithm. *IEEE J. Sel. Top. Appl. Earth Obs. Remote Sens.* **2020**, *13*, 620–631. [CrossRef]
26. Chen, R.; Li, W.; Zhang, Y.; Yang, J. Forward Looking Imaging of Airborne Multichannel Radar based on Modified IAA. In Proceedings of the IGARSS 2022—2022 IEEE International Geoscience and Remote Sensing Symposium, Kuala Lumpur, Malaysia, 17–22 July 2022; pp. 2987–2990. [CrossRef]
27. Guo, Y.; Zhang, D.; Li, Q.; Zhang, P.; Liang, Y. FIAA-Based Super-Resolution Forward-Looking Radar Imaging Method for Maneuvering Platforms. In Proceedings of the 2022 3rd China International SAR Symposium (CISS), Shanghai, China, 2–4 November 2022; pp. 1–5. [CrossRef]
28. Coutts, S.; Cuomo, K.; McHarg, J.; Robey, F.; Weikle, D. Distributed coherent aperture measurements for next generation BMD radar. In Proceedings of the Fourth IEEE Workshop on Sensor Array and Multichannel Processing, Waltham, MA, USA, 12–14 July 2006; IEEE: New York, NY, USA, 2006; pp. 390–393. [CrossRef]
29. CHEN, J.; WANG, T.; WU, J.; LIU, X. Airborne distributed coherent aperture radar synchronization error calibration method based on prominent points. *J. Electron. Inf. Technol.* **2021**, *43*, 356–363. [CrossRef]
30. Baoliang, Z.; Dongming, Z.; Hongwei, G.; Yaobing, L. Test and analysis of distributed aperture coherence-synthetic radar technology. *J. Terahertz Sci. Electron. Inf. Technol.* **2019**, *17*, 413–417. [CrossRef]
31. Liang, C.; Li, Y.; Hu, X.; Wang, Y.; Zhang, L.; Wang, M.; Guo, J. Coherent-on-receive synthesis using dominant scatterer in millimeter-wave distributed coherent aperture radar. *Remote Sens.* **2023**, *15*, 1505. [CrossRef]
32. Dai, F.; Li, Y.; Wang, Y.; Chen, H. Efficient Implementation for SBL-Based Coherent Distributed mmWave Radar Imaging. *Remote Sens.* **2023**, *15*, 1054. [CrossRef]
33. Krieger, G.; Younis, M. Impact of oscillator noise in bistatic and multistatic SAR. *IEEE Geosci. Remote Sens. Lett.* **2006**, *3*, 424–428. [CrossRef]
34. Kenney, R.H.; Metcalf, J.G.; McDaniel, J.W. Wireless Distributed Frequency and Phase Synchronization for Mobile Platforms in Cooperative Digital Radar Networks. *IEEE Trans. Radar Syst.* **2024**, *2*, 268–287. [CrossRef]

35. Merlo, J.M.; Schlegel, A.; Nanzer, J.A. High Accuracy Wireless Time-Frequency Transfer For Distributed Phased Array Beamforming. In Proceedings of the 2023 IEEE/MTT-S International Microwave Symposium—IMS 2023, San Diego, CA, USA, 11–16 June 2023; pp. 109–112. [CrossRef]
36. Mghabghab, S.R.; Nanzer, J.A. Open-Loop Distributed Beamforming Using Wireless Frequency Synchronization. *IEEE Trans. Microw. Theory Tech.* **2021**, *69*, 896–905. [CrossRef]
37. Yulin, H.; Jianyu, Y.; Junjie, W.; Jintao, X. Precise time frequency synchronization technology for bistatic radar. *J. Syst. Eng. Electron.* **2008**, *19*, 929–933. [CrossRef]
38. Wang, W.Q. GPS-Based Time & Phase Synchronization Processing for Distributed SAR. *IEEE Trans. Aerosp. Electron. Syst.* **2009**, *45*, 1040–1051. [CrossRef]
39. Pu, W.; Li, W.; Lv, Y.; Wang, Z. An extended omega-K algorithm with integrated motion compensation for bistatic forward-looking SAR. In Proceedings of the 2015 IEEE Radar Conference (RadarCon), Arlington, VA, USA, 10–15 May 2015; pp. 1291–1295. [CrossRef]
40. Ying-jie, Z.; Yan-ping, W.; TAN, W.; Hong, W. Research on Motion Compensation for Airborne Forward Looking Synthetic Aperture Radar with Linear Array Antennas. *J. Radars* **2013**, *2*, 168. [CrossRef]
41. Liu, D.; Kamilov, U.S.; Boufounos, P.T. Coherent distributed array imaging under unknown position perturbations. In Proceedings of the 2016 4th International Workshop on Compressed Sensing Theory and its Applications to Radar, Sonar and Remote Sensing (CoSeRa), Aachen, Germany, 19–22 September 2016; pp. 105–109. [CrossRef]
42. Karlsson, J.; Rowe, W.; Xu, L.; Glentis, G.O.; Li, J. Fast missing-data IAA with application to notched spectrum SAR. *IEEE Trans. Aerosp. Electron. Syst.* **2014**, *50*, 959–971. [CrossRef]
43. Stoica, P.; Li, J.; Ling, J.; Cheng, Y. Missing data recovery via a nonparametric iterative adaptive approach. In Proceedings of the 2009 IEEE International Conference on Acoustics, Speech and Signal Processing, Taipei, Taiwan, 19–24 April 2009; IEEE: New York, NY, USA, 2009; pp. 3369–3372. [CrossRef]
44. Moore, T.G.; Zuerndorfer, B.W.; Burt, E.C. Enhanced imagery using spectral-estimation-based techniques. *Linc. Lab. J.* **1997**, *10*, 171–186.
45. Rambach, K.; Yang, B. MIMO radar: Time division multiplexing vs. code division multiplexing. In Proceedings of the International Conference on Radar Systems (Radar 2017), Belfast, Ireland, 23–26 October 2017; IET: London, UK, 2017; pp. 1–5. [CrossRef]
46. Tucker, R.S.; Eisenstein, G.; Korotky, S.K. Optical time-division multiplexing for very high bit-rate transmission. *J. Light. Technol.* **1988**, *6*, 1737–1749. [CrossRef]
47. Bellettini, A.; Pinto, M.A. Theoretical accuracy of synthetic aperture sonar micronavigation using a displaced phase-center antenna. *IEEE J. Ocean. Eng.* **2002**, *27*, 780–789. [CrossRef]
48. Donnet, B.; Longstaff, I. MIMO radar, techniques and opportunities. In Proceedings of the 2006 European Radar Conference, Manchester, UK, 13–15 September 2006; IEEE: New York, NY, USA, 2006; pp. 112–115. [CrossRef]
49. Li, S.; Wang, S.; An, Q.; Zhao, G.; Sun, H. Cylindrical MIMO Array-Based Near-Field Microwave Imaging. *IEEE Trans. Antennas Propag.* **2021**, *69*, 612–617. [CrossRef]
50. Li, N.; Wang, R.; Deng, Y.; Chen, J.; Zhang, Z.; Liu, Y.; Xu, Z.; Zhao, F. Improved full-aperture ScanSAR imaging algorithm based on aperture interpolation. *IEEE Geosci. Remote Sens. Lett.* **2015**, *12*, 1101–1105. [CrossRef]
51. Ning, J.; Liu, D.; Liu, K.; Zhang, H.; Wang, Y. An Improved Full-Aperture ScanSAR Imaging Method Integrating the MIAA Based Aperture Interpolation. *J. Sensors* **2020**, *2020*, 8196081. [CrossRef]
52. Yardibi, T.; Li, J.; Stoica, P.; Xue, M.; Baggeroer, A.B. Source Localization and Sensing: A Nonparametric Iterative Adaptive Approach Based on Weighted Least Squares. *IEEE Trans. Aerosp. Electron. Syst.* **2010**, *46*, 425–443. [CrossRef]
53. Li, J.; Stoica, P.; Wang, Z. On robust Capon beamforming and diagonal loading. *IEEE Trans. Signal Process.* **2003**, *51*, 1702–1715. [CrossRef]
54. Schmidt, R. Multiple emitter location and signal parameter estimation. *IEEE Trans. Antennas Propag.* **1986**, *34*, 276–280. [CrossRef]
55. Wang, J.; Kwon, S.; Shim, B. Generalized Orthogonal Matching Pursuit. *IEEE Trans. Signal Process.* **2012**, *60*, 6202–6216. [CrossRef]
56. Beck, A.; Teboulle, M. A fast iterative shrinkage-thresholding algorithm for linear inverse problems. *SIAM J. Imaging Sci.* **2009**, *2*, 183–202. [CrossRef]
57. Iqbal, M.; Chen, J.; Yang, W.; Wang, P.; Sun, B. Kalman filter for removal of scalloping and inter-scan banding in scansar images. *Prog. Electromagn. Res.* **2012**, *132*, 443–461. [CrossRef]
58. Romeiser, R.; Horstmann, J.; Graber, H. A new scalloping filter algorithm for scansar images. In Proceedings of the 2010 IEEE International Geoscience and Remote Sensing Symposium, Honolulu, HI, USA, 25–30 July 2010; IEEE: New York, NY, USA, 2010; pp. 4079–4082. [CrossRef]
59. Instruments, T. Imaging Radar Using Cascaded Mmwave Sensor Reference Design. 2020. Available online: https://www.ti.com/lit/ug/tiduen5a/tiduen5a.pdf (accessed on 1 June 2024).


**Disclaimer/Publisher's Note:** The statements, opinions and data contained in all publications are solely those of the individual author(s) and contributor(s) and not of MDPI and/or the editor(s). MDPI and/or the editor(s) disclaim responsibility for any injury to people or property resulting from any ideas, methods, instructions or products referred to in the content.